Contents lists available at ScienceDirect

Journal of Sound and Vibration

An efficient model for predicting the sound radiation from a railway rail accounting for cross-section deformation

Christopher Knuth [*], Giacomo Squicciarini, David Thompson

Institute of Sound and Vibration Research, University of Southampton, Southampton, UK

A B S T R A C T

The track is the main contributor to railway rolling noise below 2 kHz. In this frequency range it is usually acceptable to represent the rail vibration using a Timoshenko beam. At higher frequencies, however, cross-section deformation occurs in the rail, which requires more complex track models. In this paper a vibroacoustic 2.5D Finite Element and Boundary Element model of a continuously supported rail is implemented for studying the effect of cross-section deformation on sound radiation. A novel interpolation strategy is developed to significantly reduce the solution time by interpolating element coefficient vectors. Results are calculated for vertical or lateral excitation applied to the rail head and comparisons are made with a Timoshenko beam model in which the cross-section remains undeformed. For vertical excitation, the sound power from both models is identical below 3 kHz, while for lateral excitation, the Timoshenko beam has differences of up to 25 dB below 200 Hz owing to the missing rail torsion and foundation eccentricity. Above 3 kHz for vertical excitation and from 1 kHz for lateral excitation, higher-order waves contribute to the sound power, causing an underestimation of up to 15 dB if the cross-section deformation is neglected. The calculated transfer functions of rail sound power per unit squared force are incorporated in a rolling noise prediction model that includes vertical and lateral dynamics. The results show that the Timoshenko beam rail underestimates the rail sound power by up to 5 dB in comparison with the 2.5D rail model in one-third octave bands.

1. Introduction

Rolling noise is the main source of noise in railways for conventional train speeds and the contribution of the track is usually dominant in the frequency range below 2 kHz, while the wheel contribution is important at higher frequencies [1]. In this frequency range below 2 kHz it is usually acceptable to represent the rail vibration using a Timoshenko beam, which neglects the effect of rail cross-section deformation. However, such cross-section deformation becomes significant at higher frequencies, so excluding this effect could potentially underestimate the sound radiated from the rail at high frequencies, leading to incorrect rolling noise predictions. In the context of rolling noise auralisation, a rail model that is accurate at high frequencies can improve the quality of the synthesised pass-by signals [2,3].

Several modelling approaches for modelling a railway track have been proposed, depending on the frequency range of interest. Knothe and Grassie [4] developed a dynamic railway track model consisting of an infinite Euler-Bernoulli or Timoshenko beam on a double-layer foundation formed by the rail pad, a sleeper and the ballast. The Timoshenko rail model of Grassie [5] can be used for studying vertical or lateral vibrations, assuming they are uncoupled and that the rail cross-section remains rigid. For vertical rail

---

vibration, this is a suitable approximation of the point mobility below 4 kHz [1]. It was also implemented in the Track-Wheel Interaction Noise Software (TWINS), see [6,7], where the vertical/lateral coupling is approximated as weighted average of the vertical and lateral rail receptances [8].

To approximate the cross-section deformation in the rail, Wu and Thompson [9,10] employed multiple beam models, linking two Timoshenko beams representing the rail foot and head linked via a layer of springs. For the lateral vibration, the web was represented by an array of vertical beams that couple the rotations of the rail head and foot.

Kostovasilis et al. [11] developed a semi-analytical track model that combines Timoshenko beam theory for vertical/lateral bending with the theories of a rod (torsional waves) and a bar (axial waves) allowing for an elastic support. By including torsion, allowing for the eccentricity of the foundation, and applying an off-centre excitation, they could observe different wave types in the vertical or lateral rail responses, which would not be predicted with the classical Timoshenko rail model from [5].

Modelling a section of the track using conventional 3D Finite Elements (FE) can lead to a model with many degrees of freedom (DoFs), as the rail has to be discretised with sufficient elements over its cross-section and needs a sufficient length to approximate an infinite rail and capture the relevant waves at high frequencies. Nielsen et al. [12] used beam elements to approximate an infinitely supported rail from a finite-length FE model. To minimise interference with reflections coming from the ends, the track needed to be sufficiently long to ensure the propagating waves have decayed away sufficiently. To minimise the reflections and allow a shorter rail section to be modelled, Yang and Thompson [13] applied a non-reflective termination via damped tapered beam elements to the rail ends.

The analytical or FE models based on beams cannot rigorously include rail cross-section deformation, thus, omitting the higher-order waves, which makes them unsuitable for high frequency rail computations. To overcome these limitations, semi-analytical FE approaches have been employed. They take advantage of the invariant rail cross-section. Two different approaches exist: Thompson [14] applied periodic structure theory, see Mead [15], to form an infinite rail from only a short section; this approach is also known as the Wave Finite Element, see Mace et al. [16]. In the 2.5D FE method, as used e.g. by Gavric [17] or Gry [18], the rail cross-section is modelled in two dimensions (2D), assuming wave propagation in the third direction. By applying a spatial Fourier transformation to the equation of motion (EoM), the information in the infinite third direction is retained in the wavenumber domain. Hence the approach is termed as 2.5D.

Nilsson et al. [19] combined the 2.5D FE with a 2.5D Boundary Element (BE) model, which was used for calculating the sound radiation of an infinite rail with an elastic single-layer support representing a rail pad and an embedded tram rail. Similar 2.5D modelling procedures have since been employed in several studies related to vibration and sound radiation of a railway track [2, 20–24].

The simulations with the 2.5D BE model can become computationally expensive, as it needs to be solved repeatedly for a large range of frequency/wavenumber combinations. Unlike an FE model, the BE model requires re-assembly of the fully populated matrices for each combination. In their model of a rail above an absorptive ballast layer, therefore, Ryue et al. [21] limited their solution to the wavenumber of the dominant wave, omitting other waves that are present. Theyssen et al. [25] proposed an interpolation method that they used to calculate acoustic transfer functions per unit velocity on each element for evaluating the sound field around a rail. In their method, results obtained for a fixed set of frequency/wavenumber combinations are mapped and re-scaled between different combinations. A similar interpolation approach was proposed by Thompson et al. [26]. However, neither approach allows for frequency-dependent boundary conditions, e.g. for including absorptive properties of the railway ballast.

In [2], Theyssen compared the sound power radiated by a continuously or discretely supported Timoshenko beam and 2.5D FE rail for a vertical unit force applied at the rail centre or off-centre in one-third octave bands. An underestimation of up to 10 dB was found in some bands, when using the Timoshenko beam, suggesting the 2.5D FE rail on average radiates more sound power. However, the influence of cross-section deformation on rolling noise was not specifically addressed, and lateral excitation of the Timoshenko beam was not considered.

In this paper the effect of rail cross-section deformation on the radiated sound power is assessed by comparison of the normalised sound power per unit force squared obtained from a 2.5D BE model using a 2.5D FE rail and Timoshenko beam rail model for calculating the vertical and lateral vibration input in the vibroacoustic simulations. To achieve this, an efficient way of solving the 2.5D BE model is introduced, in which the solution times are significantly reduced by interpolation of the element coefficient vectors instead of requiring a recalculation at each computation. This approach is more versatile compared with existing literature (e.g. [21,25]) as it allows for frequency-dependent boundary conditions and fast calculations up to high frequencies with a narrow resolution. The results allow for a thorough investigation of the effect of the cross-section deformation on the rail sound power in rolling noise calculations.

The remainder of this paper is structured as follows. In Section 2, the vibroacoustic model of a supported railway track is described that combines the 2.5D FE and 2.5D BE methods to evaluate the vibration and sound radiation from the rail. In Section 3, methods for efficient solving of 2.5D FE and BE models are proposed. The vibration of the rail is investigated in Section 4, by studying the dispersion characteristics of different waves and examining the frequency responses for different types of excitation, after the experimental validation of the model. In Section 5, the effect of rail cross-section deformation on vibration and sound radiation is evaluated by a comparison of the 2.5D FE rail with a Timoshenko beam rail model. In Section 6, both rail models are used in rolling noise predictions to assess the effects in overall terms.

2. Vibroacoustic 2.5D model of the supported railway track

In this section, the numerical model used to calculate the vibration and sound radiation from the rail in a ballasted railway track is presented using the 2.5D FE and 2.5D BE methods. These approaches assume the rail is an infinite waveguide with an invariant cross-section.

The coordinates adopted in the 2.5D models can be seen in Fig. 1, showing the mesh of the rail. It consists of 126 quadratic finite elements with 1413 DoFs. A foundation is applied to the boundary Γ_f at the bottom of the rail foot. The meshes of the 2.5D FE and BE models coincide on the boundary Γ of the rail perimeter. The BE mesh consists of 92 quadratic boundary elements, the size of which is chosen to ensure that there are at least four elements per acoustic wavelength at the highest frequency of interest, set to 10 kHz in the following studies. Besides, the excitation point N_1 at the rail head centre and a position on the rail foot N_2 at which vibration is additionally observed, are marked.

2.1. The 2.5D Finite Element model of the rail

For modelling the rail vibration, the 2.5D FE approach is used [17,19]. The structure is modelled in 2D in the y-z plane, assuming time-harmonic wave propagation in the x-direction. Consequently, the displacement field can be decomposed as

$$\mathbf{u}(x, y, z, \omega) = \left\{ \begin{array}{c} u_x(y, z) \\ u_y(y, z) \\ u_z(y, z) \end{array} \right\} e^{-i\kappa x} e^{i\omega t} \tag{1}$$

where $u_x(y,z)$, $u_y(y, z)$ and $u_z(y, z)$ are the displacement amplitudes in the x-, y- and z-direction in the 2D y-z plane, κ is the longitudinal wavenumber in the x-direction in which the waves propagate, and ω is the circular frequency.

Following the derivation in [17,19], the EoM in the spatial domain can be written as

$$\left(\frac{\partial^2}{\partial x^2} \mathbf{K}_2 + \frac{\partial}{\partial x} \mathbf{K}_1 + \mathbf{K}_0 + \mathbf{K}_f - \omega^2 \mathbf{M} \right) \mathbf{u}(x) = \mathbf{f}(x), \tag{2}$$

where $\mathbf{K}_2$, $\mathbf{K}_1$ and $\mathbf{K}_0$ are the stiffness matrices, $\mathbf{K}_f$ is the foundation stiffness matrix, and $\mathbf{M}$ is the mass matrix of the structure, $\mathbf{u}$ and $\mathbf{f}$ are the vectors of the nodal displacement and force amplitudes. The definition of the matrices, except $\mathbf{K}_f$, can be found in the above references and they are assembled using the FE procedure [27]. The foundation stiffness matrix $\mathbf{K}_f$ represents the rail support and will be introduced in Section 2.2. Damping in the rail is included by means of a complex Young's modulus $E(1 + i\eta)$ with a constant loss factor η.

By defining the spatial Fourier transform pairs of the displacements in the x-direction as

$$\widetilde{\mathbf{u}}(\kappa) = \int_{-\infty}^{\infty} \mathbf{u}(x) e^{i\kappa x} dx \quad \text{and} \quad \mathbf{u}(x) = \frac{1}{2\pi} \int_{-\infty}^{\infty} \widetilde{\mathbf{u}}(\kappa) e^{-i\kappa x} d\kappa, \tag{3}$$

and likewise those of the force as

$$\widetilde{\mathbf{f}}(\kappa) = \int_{-\infty}^{\infty} \mathbf{f}(x) e^{i\kappa x} dx \quad \text{and} \quad \mathbf{f}(x) = \frac{1}{2\pi} \int_{-\infty}^{\infty} \widetilde{\mathbf{f}}(\kappa) e^{-i\kappa x} d\kappa, \tag{4}$$
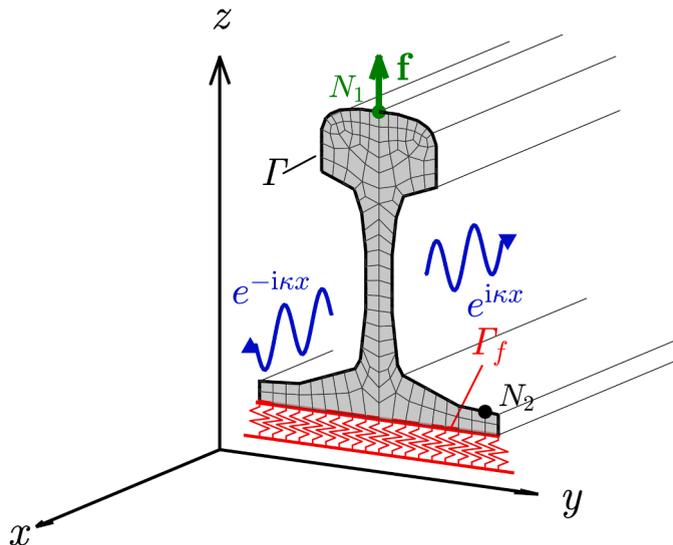

Fig. 1. Coordinate system in the 2.5D FE/BE model of the supported rail; • rail head centre node N_1 (excitation point); •, rail foot node N_2.

the EoM in Eq. (2) can be expressed in the wavenumber domain as

$$\left[(-\mathrm{i}\kappa)^2\mathbf{K}_2 + (-\mathrm{i}\kappa)\mathbf{K}_1 + \mathbf{K}_0 + \mathbf{K}_f - \omega^2\mathbf{M}\right]\widetilde{\mathbf{u}}(\kappa) = \widetilde{\mathbf{f}}(\kappa). \tag{5}$$

By setting $\widetilde{\mathbf{f}}(\kappa) = 0$ in Eq. (5), an eigenvalue problem (EVP) can be obtained that is linear in ω^2 or quadratic in $(-\mathrm{i}\kappa)$, which can be used to obtain the results for free wave propagation in the rail. Solving the linear EVP in ω^2 is straightforward; moreover, by setting $\kappa = 0$, the cut-on frequencies $f_c = \omega_c/2\pi$ of the waves in the rail can be obtained [17].

In this application, the quadratic EVP needs to be solved to calculate the forced response for a given ω, which can be achieved by applying a linearisation of the quadratic EVP as

$$\left(\begin{bmatrix} 0 & \mathbf{K}_0 + \mathbf{K}_f - \omega^2\mathbf{M} \\ \mathbf{K}_0 + \mathbf{K}_f - \omega^2\mathbf{M} & \mathbf{K}_1 \end{bmatrix} - \lambda \begin{bmatrix} \mathbf{K}_0 + \mathbf{K}_f - \omega^2\mathbf{M} & 0 \\ 0 & -\mathbf{K}_2 \end{bmatrix}\right) \left\{\begin{matrix} \boldsymbol{\phi}_n \\ \lambda\boldsymbol{\phi}_n \end{matrix}\right\} = 0, \tag{6}$$

where λ is the eigenvalue, which yields the wavenumber of the n-th wave as $\lambda = -\mathrm{i}\kappa_n$, and $\boldsymbol{\phi}_n$ is the corresponding eigenvector that contains the wave shape. In a damped waveguide ($\eta \neq 0$), the wavenumbers are generally complex $\kappa_n = \pm\kappa_{\mathrm{re}} \pm \mathrm{i}\kappa_{\mathrm{im}}$ and occur in doublets or quadruples, where the real part $\pm\kappa_{\mathrm{re}}$ corresponds to the wavenumber of wave propagation in the positive or negative direction and the imaginary part $-\kappa_{\mathrm{im}}$ corresponds to the rate of decay. Thus, the wave solutions correspond to propagating, evanescent, or evanescent oscillating waves that propagate or decay in the positive and negative directions [17].

To recover the response in the spatial domain, the inverse Fourier transform in Eq. (3) is replaced by a contour integration enclosing N poles at the wavenumbers of the $2N$ waves. The N poles corresponding to waves propagating towards $+x$ lie in the upper complex half plane ($\kappa_{\mathrm{im}} > 0$) and the other N propagating in direction of $-x$ are in the lower half-plane ($\kappa_{\mathrm{im}} < 0$). The forced response is then calculated as [28]

$$\mathbf{u}(x) = \pm\mathrm{i}\sum_{n=1}^{N}\frac{\boldsymbol{\phi}_n^L\widetilde{\mathbf{f}}(\kappa)}{\boldsymbol{\phi}_n^L(-\mathrm{i}\mathbf{K}_1 - 2\kappa_n\mathbf{K}_2)\boldsymbol{\phi}_n^R}\boldsymbol{\phi}_n^R\mathrm{e}^{-\mathrm{i}\kappa_n x}, \tag{7}$$

where $\boldsymbol{\phi}_n^L$ and $\boldsymbol{\phi}_n^R$ are the left and right eigenvectors of the n-th wave corresponding to wavenumber κ_n; if $x \leq 0$ the positive sign is used, and for $x \geq 0$ the negative sign is used instead, and the summation is over the respective set of N poles. At each circular frequency ω, the forced response can thus be determined using the wave solutions obtained from Eq. (6). By multiplication with $\mathrm{i}\omega$ or $(\mathrm{i}\omega)^2$, the velocity ($\dot{\mathbf{u}}$) or acceleration ($\ddot{\mathbf{u}}$) amplitude can be obtained. If the force amplitude is set to unity at the DoF used as driving point in the rail at $x = 0$, the frequency response function (FRF) is obtained. Here, results will be presented as mobility throughout.

The forced response in the wavenumber domain, as required for the vibroacoustic simulations with the 2.5D BE model, can be calculated as [29]

$$\widetilde{\mathbf{u}}(\kappa) = \sum_{n=1}^{2N}\frac{\boldsymbol{\phi}_n^L\widetilde{\mathbf{f}}(\kappa)}{\boldsymbol{\phi}_n^L(-\mathrm{i}\mathbf{K}_1 - 2\kappa_n\mathbf{K}_2)\boldsymbol{\phi}_n^R}\boldsymbol{\phi}_n^R\frac{1}{\kappa_n - \kappa}, \tag{8}$$

where the summation is now over all $2N$ waves.

Since the nodes on the rail perimeter in the FE mesh and the BE mesh coincide, the normal velocities $\widetilde{v}_n(\kappa) = \mathrm{i}\omega\widetilde{\mathbf{u}}(\kappa).\mathbf{n}$ can be obtained and used as input to the 2.5D BE model, where $\mathbf{n}$ is the inward pointing normal vector.

2.2. Introducing the foundation stiffness of the track support

In the supported track model, the rail is resting on a continuous elastic foundation that is applied to the rail foot, as shown in Fig. 1, which yields the foundation stiffness matrix $\mathbf{K}_f$ in the EoM in Eqs (2) and (5). Discrete support effects such as the pinned-pinned resonances are neglected in this study [1].

The matrix $\mathbf{K}_f$ is calculated by numerically distributing the dynamic support stiffness matrix $\mathbf{k}_f$ over the finite element nodes along Γ_f, which coincide with the rail foot. A double-layer support consisting of a rail pad in series with a ballasted sleeper is used, for which the dynamic stiffness matrix (per unit length) is given as

$$\mathbf{k}_f = \frac{1}{d}\left(\boldsymbol{\alpha}_p + \boldsymbol{\alpha}_s\right)^{-1}, \tag{9}$$

where $\boldsymbol{\alpha}_p$ and $\boldsymbol{\alpha}_s$ are the receptance matrices of the rail pad and the ballasted sleeper which have a size of 3×3, as each node has 3 DoFs, and d is the distance between the supports.

The sleeper DoFs need to be coupled to the corresponding rail DoFs at the nodes of the rail foot Γ_f, to assemble the global foundation stiffness matrix $\mathbf{K}_f$. Equation (9) allows a rigid sleeper or a flexible sleeper model to be used. In this paper, the sleeper is represented as a Timoshenko beam embedded in ballast, using the model developed by Kostovasilis [30]. This model is used to calculate $\boldsymbol{\alpha}_s$ at the rail seat location on the sleeper, assuming a single point connection to the sleeper. Damping in the rail pad is included via a complex stiffness $k_p(1 + \mathrm{i}\eta_p)$, where η_p is the loss factor of the rail pad, while in the ballast a viscous damper is added as $k_b + \mathrm{i}\omega c_b$, where c_b is the ballast damping coefficient. The viscous damper is preferred here, as it better represents the dynamic stiffness of the ballast at high

frequencies [31].

2.3. Timoshenko beam model of the rail

To assess the effect of rail cross-section deformation, the 2.5D FE model is compared with a Timoshenko beam model of the rail, in which higher-order waves and cross-section deformation of the rail are neglected.

Following the structure of the EoM of the 2.5D model given in Eq. (6), the EoM of the Timoshenko beam after transforming to the frequency/wavenumber domain can be written as [30]

$$\left((-i\kappa)^2 \begin{bmatrix} -GA\gamma & 0 \\ 0 & EI \end{bmatrix} + (-i\kappa) \begin{bmatrix} 0 & GA\gamma \\ -GA\gamma & 0 \end{bmatrix} + \begin{bmatrix} EI & 0 \\ 0 & GA\gamma \end{bmatrix} + \begin{bmatrix} k_f & 0 \\ 0 & k_{f,r} \end{bmatrix} - \omega^2 \begin{bmatrix} \rho A & 0 \\ 0 & \rho I \end{bmatrix} \right) \left\{ \begin{array}{c} \widetilde{u}(\kappa) \\ \widetilde{\psi}(\kappa) \end{array} \right\} = \left\{ \begin{array}{c} \widetilde{f}(\kappa) \\ \widetilde{m}(\kappa) \end{array} \right\}, \tag{10}$$

where A is the cross-section area and I second moment of area of the rail, ρ is the density, E the Young's modulus and G the shear modulus of the material, γ is the shear correction, k_f and $k_{f,r}$ are the translational and rotational dynamic stiffness per unit length of the track support. Equation (10) is used for both vertical and lateral vibration. The classic Timoshenko beam model only allows for a translation and a rotation DoF, $\widetilde{u}$ and $\widetilde{\psi}$, respectively, for either vertical bending ($\widetilde{u}_z$ and ψ_y) or lateral bending ($\widetilde{u}_y$ and ψ_z). Both beam equations need to be solved separately for a unit force input in either vertical ($\widetilde{f}_z = 1$ N) or lateral ($\widetilde{f}_y = 1$ N) direction, setting the torques to zero $\widetilde{m}_y = \widetilde{m}_z = 0$. As before, rail damping is included by using a complex Young's modulus $E(1 + i\eta)$.

Writing the Timoshenko beam equation in the frequency/wavenumber domain allows the same solution procedures to be used to solve the EoM as in Section 2.1. The resulting vertical or lateral velocities per unit force are applied to each node of the BE mesh for the vibroacoustic simulations with the 2.5D BE model, after resolving them in the normal direction. In this way, the results of the Timoshenko beam rail can be compared with the 2.5D FE rail.

2.4. The 2.5D Boundary Element model of the rail

For modelling the 3D sound field generated by the rail, the 2.5D BE method is used. Similar to the displacement in the 2.5D FE method, see Eq. (3), the sound pressure p can be written as a Fourier transform pair

$$\widetilde{p}(\kappa) = \int_{-\infty}^{\infty} p(x)e^{i\kappa x}dx \quad \text{and} \quad p(x) = \frac{1}{2\pi} \int_{-\infty}^{\infty} \widetilde{p}(\kappa)e^{-i\kappa x}d\kappa, \tag{11}$$

and likewise, the normal particle velocity v_n (or pressure gradient $dp/dn = -i\omega\rho_0 v_n$). In the 2.5D approach, classic 2D BE problems governed by the 2D Kirchhoff-Helmholtz integral equation need to be solved over a range of wavenumbers α in the 2D plane given by [19]

$$\alpha = \sqrt{k^2 - \kappa^2}, \tag{12}$$

which is the in-plane component of the wavenumber in air $k = 2\pi f/c_0$, with the speed of sound $c_0 = 343$ m/s. For each frequency f, the calculations are repeated for a range of longitudinal wavenumbers κ. For the case in which $k > \kappa$, α is real and the sound field consists of propagating waves, i.e. sound is radiated into the far-field. On the contrary, if $k < \kappa$, α is imaginary which produces exponentially decaying near-fields in the y-z plane. If $k = \kappa$, the radiated sound power would theoretically tend to infinity [32], thus, this case is excluded from the calculations [33].

The 2.5D boundary integral equation governing the sound radiation into an unbounded exterior fluid domain is

$$C(\mathbf{y})\widetilde{p}(\kappa, \mathbf{y}) = -\int \left(i\omega\rho_0 G(\kappa, \mathbf{y}|\mathbf{x})\widetilde{v}_n(\kappa, \mathbf{x}) + \widetilde{p}(\kappa, \mathbf{x}) \frac{\partial G(\kappa, \mathbf{y}|\mathbf{x})}{\partial n} \right) d\Gamma, \tag{13}$$

where $\widetilde{p}(\kappa, \mathbf{y})$ is the sound pressure at the field position $\mathbf{y}(y, z)$ in the fluid domain, $\widetilde{v}_n(\kappa, \mathbf{x})$ and $\widetilde{p}(\kappa, \mathbf{x})$ are the normal velocity and sound pressure at a position $\mathbf{x}(y_\Gamma, z_\Gamma)$ on the boundary Γ of the vibrating structure, $\rho_0 = 1.21$ kg/m^3 is the density of air, $G(\kappa, \mathbf{y}|\mathbf{x})$ and $\partial G(\kappa, \mathbf{y}|\mathbf{x})/\partial n$ are the Green's function and its normal derivative, that determine the response at field position $\mathbf{y}$ for a source located at $\mathbf{x}$, and $C(\mathbf{y})$ is a coefficient that depends on the position $\mathbf{y}$ of the receiver. Thus, knowing $\widetilde{v}_n(\kappa, \mathbf{x})$ and $\widetilde{p}(\kappa, \mathbf{x})$ on the boundary Γ, allows the sound pressure $\widetilde{p}(\kappa, \mathbf{y})$ to be calculated at any field position $\mathbf{y}$ in the 2D plane and wavenumber domain. From the sound pressure $\widetilde{p}(\kappa, \mathbf{y})$ in the wavenumber domain, the solution in the spatial domain $p(x,\mathbf{y})$, i.e. along the rail, can be obtained via the inverse Fourier integral given in Eq. (11). The range of κ needs to be set sufficiently large, including solutions with real and imaginary α, to ensure a correct calculation of the sound pressure $p(x,\mathbf{y})$ at any receiver position $\mathbf{y}$ in the near- or far-field.

The fundamental solution of the 2D wave equation can be employed as Green's function in the 2.5D BE integral equation as [19]

$$G = -\frac{i}{4}H_0^{(2)}(\alpha r) \quad \text{and} \quad \frac{\partial G}{\partial n} = \frac{i\alpha}{4}H_1^{(2)}(\alpha r)\frac{\partial r}{\partial n}, \tag{14}$$

where $H_0^{(2)}$ and $H_1^{(2)}$ are Hankel functions of the second kind and order 0 and 1, respectively, $r = |\mathbf{x} - \mathbf{y}|$ is the distance between the

source and receiver, and $\partial r/\partial n$ its normal derivative. The difference from the classic 2D Green's function, e.g. found in [34], is that the wavenumber k is replaced with α [19].

The Green's function given in Eq. (14) can be used for the case where $k > \kappa$ with a real-valued α. To include the exponentially decaying near-field solutions with an imaginary-valued α, i.e. $k < \kappa$, a near-field Green's function was defined in [33] as

$$G = \frac{1}{2\pi}K_0(r\beta) \quad \text{and} \quad \frac{\partial G}{\partial n} = -\frac{\beta}{2\pi}K_1(r\beta)\frac{\partial r}{\partial n}, \tag{15}$$

where K_0 and K_1 are the modified Bessel functions of the second kind and order 0 and 1, respectively, and their argument β is defined as $\beta = \sqrt{\kappa^2 - k^2}$. This Green's function is essentially valid for all cases [33], i.e. $k < \kappa$ ($\beta = -i\alpha$) and $k > \kappa$ ($\beta = i\alpha$), and can replace Eq. (14). A rigid ground could be added in the model by adjusting the Green's function to account for the contribution of the mirror source [34].

The BE collocation process requires numerical integration of the Green's function and its normal derivative over the boundary Γ element-by-element to obtain the element coefficient vectors $\mathbf{h}^e$ and $\mathbf{g}^e$ for each collocation point, see [34]. Following this, the discretised 2.5D boundary integral equation can be written in matrix form as [34]

$$(\mathbf{C} + \mathbf{H})\mathbf{p} = -i\omega\rho_0\mathbf{G}\mathbf{v}_n, \tag{16}$$

where $\mathbf{H}$ and $\mathbf{G}$ are system matrices that contain the Green's function and its normal derivative, $\mathbf{C}$ is a diagonal matrix of the coefficients $C(\mathbf{y})$, $\mathbf{p}$ and $\mathbf{v}_n$ are the vectors of nodal sound pressure and normal velocity on the boundary.

To solve Eq. (16), boundary conditions need to be applied to the nodes of each element in the BE mesh, by specifying either a sound pressure, a normal velocity, or an impedance as the ratio between the two. One-way coupling is assumed here, which means that the vibration field in the structure is not affected by the sound field, and both can be solved separately. Since the rail is much heavier than the surrounding air, this is a reasonable approximation. Consequently, the nodal normal velocities on the boundary Γ of the 2.5D FE mesh are mapped to the 2.5D BE mesh.

By applying the boundary conditions to each element, the element coefficients $\mathbf{h}^e$ and $\mathbf{g}^e$ of the matrices in Eq. (16), can be written as a system of equations [34]

$$\mathbf{A}\mathbf{q} = \mathbf{b}, \tag{17}$$

where $\mathbf{A}$ and $\mathbf{b}$ are the system coefficient matrix and vector, and $\mathbf{q}$ is the vector of the unknown amplitudes of nodal sound pressures $\widetilde{p}$ and normal velocities $\widetilde{v}_n$ on the boundary Γ. To avoid cavity resonances in the interior of boundary Γ, ten CHIEF points are added inside the rail, to force zero sound pressure inside [35]. Consequently, the system matrix $\mathbf{A}$ is no longer square and Eq. (17) needs to be solved in a least-squares sense [34].

The sound power W radiated by the infinite rail and its spatially averaged mean square velocity $\langle \overline{v_n^2} \rangle_{\text{inf}}$ averaged over the rail perimeter are calculated by integrating the 2.5D BE solutions over the wavenumber κ and the boundary Γ as [19]

$$W = \frac{1}{2}\text{Re}\left(\int\limits_{-\kappa_0}^{\kappa_0} \int\limits_{\Gamma} \widetilde{p}^*(\kappa)\widetilde{v}_n(\kappa)\, d\Gamma d\kappa \right), \tag{18}$$

and

$$\langle \overline{v_n^2} \rangle_{\text{inf}} = \frac{1}{L}\int\limits_{-\infty}^{\infty}\int\limits_{\Gamma}\frac{1}{2}|\widetilde{v}_n(\kappa)|^2 d\Gamma d\kappa, \tag{19}$$

where L is the perimeter length of the vibrating rail in the BE mesh, over which $\widetilde{v}_n$ is averaged in Eq. (19). The integral of sound power in Eq. (18) needs to be evaluated over the whole boundary, which apart from the rail, could also include other geometries such as the train, the track, or a noise barrier. It should be noted that the integration over wavenumber in these equations corresponds to an integration in the axial direction [19]. In terms of sound power in Eq. (18), it is sufficient to integrate over wavenumbers up to κ_0, which is defined here as the largest wavenumber κ that produces positive and real-valued α at the corresponding frequency. For sound power, the near-field solution is not required, as these waves do not contribute to the far-field [19], whereas it is required for the near-field pressure. The integral over wavenumber κ in Eq. (19) is generally unbounded, but it is sufficient to extend the wavenumber range above the largest κ_n of the waves that are cut on at a given frequency. The results of both integrals converge for sufficiently closely spaced wavenumber points κ. Due to symmetry of the wavenumber spectra, the integration limits can be reduced to positive wavenumbers only, and the results multiplied by a factor of 2.

From the radiated sound power and the spatially averaged mean square velocity, the radiation efficiency of the infinite rail can be obtained as [19]

$$\sigma = \frac{W}{\rho_0 c_0 L \langle \overline{v_n^2} \rangle_{\text{inf}}}. \tag{20}$$

3. Methods for efficient solution of the 2.5D FE/BE model

To accelerate the calculation times while ensuring an accurate solution of the 2.5D FE/BE model, methods for efficient solution are proposed in this section. First an optimum distribution of wavenumbers κ is found at each frequency in terms of the vibration, which reduces the number of computations per frequency. Then, a novel interpolation method for solving sound radiation calculations from the 2.5D BE model is introduced and compared with the classic approach.

3.1. Optimisation of the wavenumber distribution

For Eqs. (18) and (19) to converge, a suitable wavenumber discretisation is required when calculating the velocity in the wavenumber domain from the 2.5D FE model with Eq. (8) as boundary condition for the 2.5D BE model. The velocity spectrum consists of peaks occurring at wavenumbers equal to the real part κ_{re} of the n-th propagating wave and their width is determined by the corresponding imaginary part κ_{im}. A wave with a high decay rate (large κ_{im}) occurs as a wide peak, while a wave with low decay rate (small κ_{im}) produces a sharp peak; the half power bandwidth in the wavenumber response can be found as $\Delta\kappa_{HP} = 2\kappa_{im}$. Therefore, rather than using a regular wavenumber discretisation which is fine enough to capture all peaks sufficiently, an irregular wavenumber spacing is introduced to reduce the overall number of computations [19,36].

To parametrise the selection of wavenumbers κ for use in the calculations, three integers are introduced, X, Y and Z. Around each wavenumber κ_n that produces a peak in the velocity spectrum, X wavenumbers are distributed between $\kappa_{re} \pm Y\kappa_{im}$ for some value Y; if $Y = 1$, the points are within the half power band and an increasing value of Y widens the band. Similar to Theyssen [36], the wavenumbers are distributed symmetrically about the peak at κ_{re} with a logarithmic spacing in the defined band, i.e. around κ_{re} there are more closely spaced points in comparison to the outer bounds $\kappa_{re} \pm Y\kappa_{im}$. Whether a wave is excited and produces a peak depends on the position and direction of the force $\tilde{\mathbf{f}}(\kappa)$ in Eq. (8) and the corresponding wave shape $\boldsymbol{\phi}_n$. To include enough wavenumber points between each peak, Z wavenumber points between $\kappa_{min} \leq \kappa \leq \kappa_{max}$ are added, here with a logarithmic spacing. This irregular wavenumber discretisation is illustrated in Fig. 2 for the spatially averaged mean square velocity $\langle v_n^2 \rangle_{inf}$ over wavenumber κ, where a single wave n with wavenumber κ_n is present, using arbitrary values $X = 30$, $Y = 14$, and $Z = 20$ for the purpose of visualisation. Any n-th wave that is propagative, i.e. produces a peak at its corresponding κ_{re} in the wavenumber spectra, can be added this way.

Depending on the material properties, the mesh, and the frequency range of interest, different combinations of the parameters X, Y, Z, κ_{min}, and κ_{max} may be sufficient. Results shown below are tailored to the rail studied in the remainder of this paper, but the above approach provides guidance for obtaining a well discretised wavenumber spectrum in general.

In the wavenumber convergence study, the parameters are set to $\kappa_{min} = 10^{-1}$ rad/m and $\kappa_{max} = 2\pi f_{max}/c_0 = 183$ rad/m, with $f_{max} = 10$ kHz, Z is varied between 50 and 300, Y is varied between 1 and 24, while X is varied between 1 and 101 (odd numbers only) to calculate the spatially averaged normal velocity from Eq. (19) over a range of frequencies. For the comparison, a reference solution with a dense regular wavenumber spacing $\Delta\kappa = \pi/c_0$ was calculated between 0 and K_{max} which ensured enough wavenumbers to reach convergence (20,001 points). Convergence needs to be ensured at each frequency, as the wavenumber spectrum changes with frequency, since real and imaginary parts κ_{re} and κ_{im} of each wavenumber κ_n are frequency-dependent. A total of 400 logarithmically spaced frequency points between $f_{min} = 10$ Hz and $f_{max} = 10$ kHz were used here. Vertical excitation is considered, but for lateral
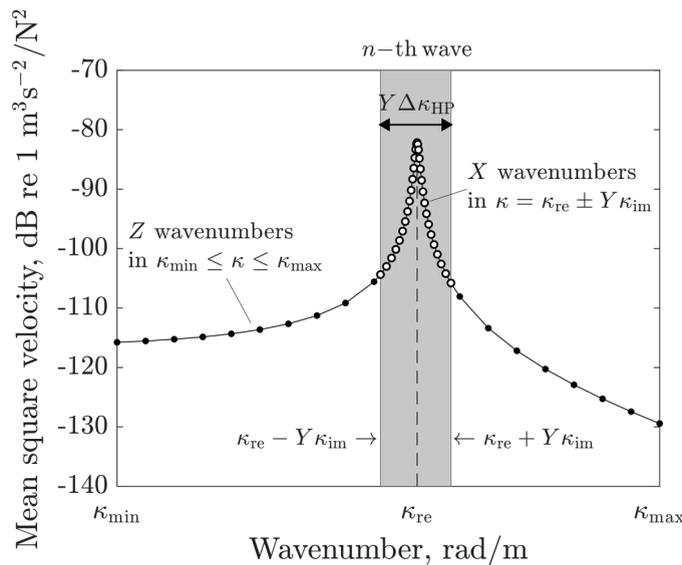

Fig. 2. Irregular wavenumber κ distribution in the band $Y\Delta\kappa_{HP}$ around the peak at κ_{re} produced by the n-th wave, using parameters $X = 30$, $Y = 14$, $Z = 20$.

excitation a similar agreement was found.

To find a minimum number of wavenumbers with the irregular κ distribution, which gives a sufficiently accurate solution but allows for an efficient calculation, the maximum error (over all frequencies) in comparison with the reference solution with a regular $\Delta\kappa$ was set to 0.1 dB. Out of all tested combinations, the optimal values of $X = 25$ and $Y = 20$ and $Z = 79$ were found, requiring 230 wavenumbers κ per frequency, with up to five propagative waves being present in the case of a vertical excitation at the rail head centre. As an example, in Fig. 3, the maximum error (over all frequencies) is shown for different values of X and Y with $Z = 79$, where the cross denotes the optimised combination. The isolines show how changes in X and Y can affect the error for this value of Z, while other values Z can show slightly different behaviour, i.e. the larger is Z, the fewer values of X may be required for a similar error with a given Y.

3.2. Solving the 2.5D BE model by an interpolation method

Solving the 2.5D BE calculations requires the BE system matrices to be computed using the Green's functions for each wavenumber α, including the wave solution in Eq. (14) and the near field solution defined in Eq. (15). This spans an infinite number of combinations of k and κ [25]. In practice, only a limited range of wavenumbers κ is required at each frequency ω to ensure convergence of the integrals in Eqs. (11), (18) and (19). Most of the computation time is required for assembling the fully populated system matrices. Making this process more efficient has the potential to reduce overall computation times. Including the near-field solution where α is imaginary can be done analogously. An interpolation method is proposed to make the 2.5D BE assembly more efficient by approximating $\mathbf{H}(\alpha)$ and $\mathbf{G}(\alpha)$ for each α. It consists of three steps:

First, the element coefficient vectors $\mathbf{h}^e(\alpha_i)$ and $\mathbf{g}^e(\alpha_i)$ are calculated for each collocation point [34] over a range of pre-defined values α_i between $\alpha_{\min} \leq \alpha_i \leq \alpha_{\max}$. The lower limit $\alpha_{\min}$ is set close to zero, as the Hankel functions $H_0^{(2)}(\alpha_i r)$ and $H_1^{(2)}(\alpha_i r)$ in Eq. (14) are not defined if their argument $\alpha_i r = 0$, while the upper limit is determined by the highest frequency of interest as $\alpha_{\max} = 2\pi f_{\max}/c_0$. The spacing between each value of α_i needs to be sufficiently narrow and depends on the largest distance $r_{\max}$, between the nodes in the BE mesh. The larger the distance r between two nodes, the faster the Hankel functions oscillate, and consequently spatial aliasing could occur if the points α_i are not sampled close enough. In the case of the near-field solution this is less of a problem, as the modified Bessel functions of the second kind in Eq. (15) are exponentially decaying if $k < \kappa$.

In the second step, from the pre-calculated element coefficients $\mathbf{h}^e(\alpha_i)$ and $\mathbf{g}^e(\alpha_i)$, the $\mathbf{h}^e(\alpha)$ and $\mathbf{g}^e(\alpha)$ for the required α are obtained by interpolation between the results for different values of α_i as

$$\mathbf{h}^e(\alpha) = \sum_{i=1}^{M} \psi_i(\alpha)\mathbf{h}^e(\alpha_i) \quad \text{and} \quad \mathbf{g}^e(\alpha) = \sum_{i=1}^{M} \psi_i(\alpha)\mathbf{g}^e(\alpha_i), \tag{21}$$

using the interpolation functions $\psi_i(\alpha)$, that are constructed from Lagrange polynomials as

$$\psi_i(\alpha) = \prod_{\substack{k=1 \\ k \neq i}}^{M} \frac{\alpha - \alpha_k}{\alpha_i - \alpha_k}, \tag{22}$$

where α_k and α_i denote the k-th and i-th wavenumber points for which $\mathbf{h}^e(\alpha_i)$ and $\mathbf{g}^e(\alpha_i)$ are pre-calculated that lie closest to the targeted
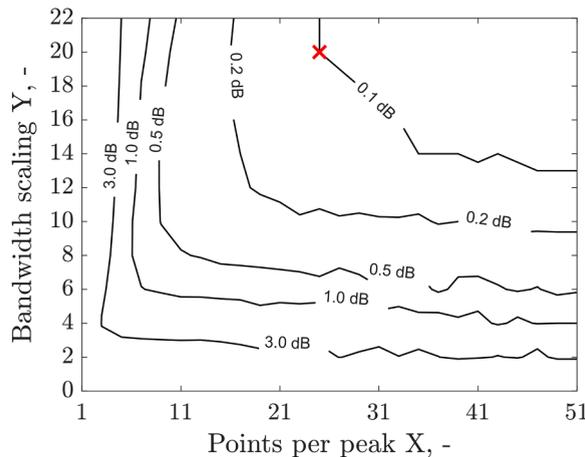
Fig. 3. Maximum error of the spatially averaged rail vibration for varying values of X (number of points per peak) and Y (bandwidth scaling around peak) with $Z = 79$ wavenumbers between $\kappa_{\min} = 10^{-1}$ rad/m and $\kappa_{\max} = 183$ rad/m; the cross ($\times$) denotes the optimised set of parameters with $X = 25$ and $Y = 20$.

α. The interpolation order ($P = M - 1$) determines the required number of points M to be used for each α. While a first order interpolation with linear polynomials ($P = 1$) requires $M = 2$ wavenumber points α_i close to α, a quartic interpolation ($P = 4$) requires $M = 5$. Hence, $\mathbf{h}^e(\alpha)$ and $\mathbf{g}^e(\alpha)$ are reconstructed between $\alpha_{\min} \leq \alpha \leq \alpha_{\max}$ by a M-point stencil of wavenumbers α_1 to α_M, that changes as α changes. If $P > 1$ and the number of α_i is small, the reconstructed function may suffer from discontinuities in the slope, but they are negligible if the number of α_i used is sufficient.

Finally, the interpolated element coefficients $\mathbf{h}^e(\alpha)$ and $\mathbf{g}^e(\alpha)$ can be inserted in the system of equations given in Eq. (17), by applying the boundary conditions to solve for $\widetilde{p}$ and $\widetilde{v}_n$. By interpolating the element coefficients, rather than the full matrices, boundary conditions can be applied to each element node, allowing for different normal vectors at nodes shared by adjacent elements. Solving Eq. (17) for each combination of k and κ enables frequency-dependent boundary conditions to be added, e.g. the velocity profile from the 2.5D FE model or the representation of an absorptive boundary defined by an acoustic impedance. This is not possible using the interpolation procedures of Theyssen or Thompson et al. [25,26], where results are calculated for unit excitation and mapped across different frequencies.

Once obtained for a given BE mesh, the element coefficients $\mathbf{h}^e(\alpha_i)$ and $\mathbf{g}^e(\alpha_i)$ can be stored and re-used for 2.5D BE calculations within the valid range of α, allowing for parametric studies to be carried out efficiently. The process of implementing the interpolation method in the 2.5D FE/BE model is illustrated in Fig. 4. Without the interpolation, the pre-calculation of the BE matrices would not be required; instead, the assembly of BE matrices is done within the nested ω-κ-loop, replacing the interpolation.

To achieve a small approximation error in the interpolation, an appropriate number N_α of values of α_i is necessary. To illustrate this, $H_1^{(2)}(\alpha_i r)$ is calculated up to a wavenumber $\alpha_{\max} = 183$ rad/m, using $r = r_{\max} = 173$ mm (from the mesh in Fig. 1) using 20 linearly spaced points of α_i and reconstructed via interpolation. The results for different orders of interpolation ($P = 1, 2, 4$) from 20 discrete α_i points are shown in Fig. 5. With a higher order of interpolation, the differences from the exact solution generally reduce. For pairs of nodes having smaller distances $r \ll r_{\max}$, better agreement can be seen, i.e. using $r_{\max}$ represents the worst case. A mesh with larger or smaller $r_{\max}$ requires a different spacing of the discrete α_i points that needs to be determined case-by-case. A more detailed error analysis is presented in Section 3.3.

To include the near-field solution where $k < \kappa$, this process would need to be repeated using Eq. (15) with the argument β instead of α, to assemble the element $\mathbf{h}^e(-i\alpha)$ and $\mathbf{g}^e(-i\alpha)$. However, since the near-field Green's function is a rapidly decaying exponential, much fewer points are already sufficient to cover the required wavenumber/frequency combinations. In the studies presented in this paper, the sound power is of interest. Hence, the near-field solutions were not included.

3.3. Error of the interpolation method

To investigate the error in the interpolation method proposed in Section 3.2, results are compared with the classic 2.5D BE solution, which requires re-assembly of the $\mathbf{H}(\alpha)$ and $\mathbf{G}(\alpha)$ matrices at each frequency/wavenumber combination. Due to the minimisation of the number of wavenumbers κ required at each frequency in Section 3.1, the 2.5D BE calculation (55k frequency/wavenumber combinations) without interpolation could be performed within reasonable time and is used here as benchmark.

The maximum error from the interpolation method is shown in Fig. 6 for different orders of interpolation ($P = 1, 2, 4$) and preassemblies of $\mathbf{h}^e(\alpha_i)$ and $\mathbf{g}^e(\alpha_i)$ for an increasing number N_α of wavenumbers α_i, which were linearly distributed between the values of $\alpha_{\min} = 10^{-3}$ rad/m and $\alpha_{\max} = 183$ rad/m, setting $f_{\min} = 10$ Hz and $f_{\max} = 10$ kHz. For linear interpolation, the solution requires
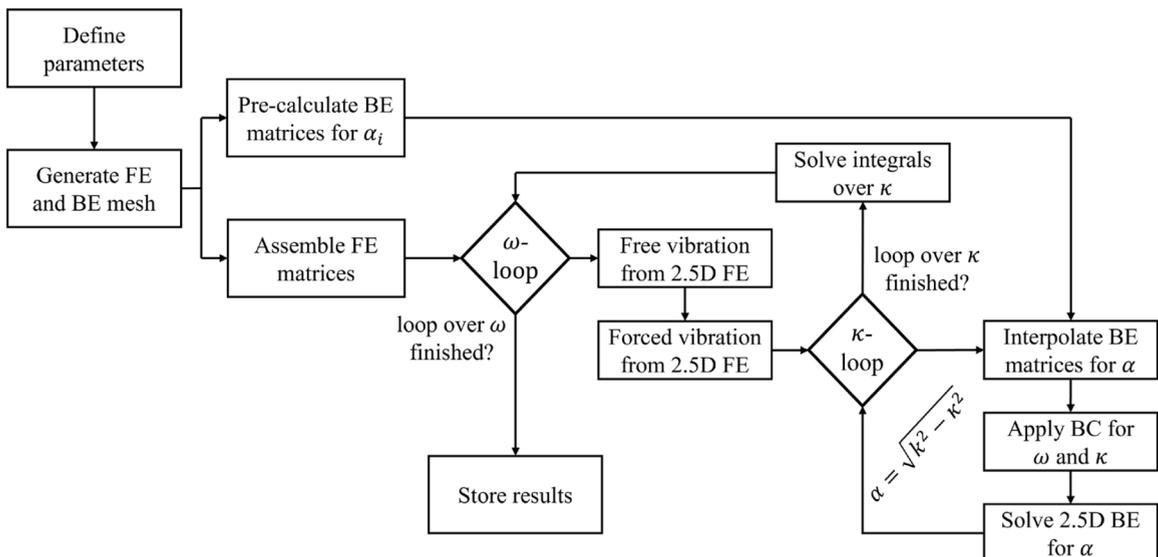

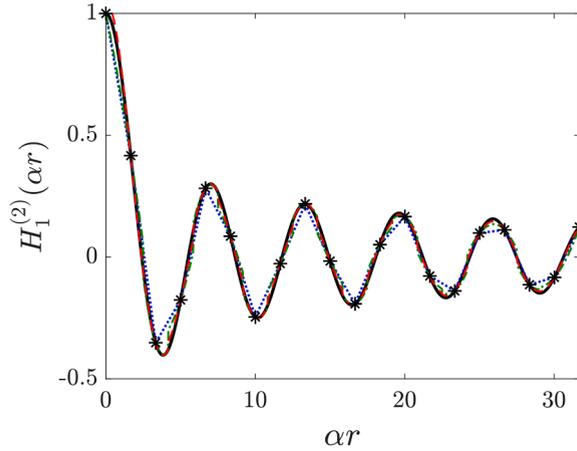**Fig. 4.** Solving the 2.5D FE/BE model using the interpolation method.

Fig. 5. Comparison of the real part of $H_1^{(2)}(\alpha r)$ with the reconstruction using $N_\alpha = 20$ values of the discrete 2D wavenumbers α_i (*) for different orders of interpolation P; ▬, continuous α (exact); ▪▪▪, linear ($P = 1$); ▬·▬, quadratic ($P = 2$); ▬ ▬, quartic ($P = 4$).

$N_\alpha \gg 300$ for convergence, while for quadratic interpolation $N_\alpha \geq 280$ is required. With a quartic interpolation the error is less than 0.1 dB if the pre-assembly is done for $N_\alpha \geq 140$. Using the interpolation method with $N_\alpha = 140$, the computation was 116 times faster in comparison with the classic method. The efficiency will be further increased, for example, if more frequency lines are studied. The solving times of both approaches will be identical, but the number of assemblies in the classic approach will be increased, while no additional pre-assemblies are required in the interpolation method.

4. Vibration of a supported railway track

The vibration of a supported rail is investigated using the models developed in Sections 2.1– 2.3. First, an experimental validation of the 2.5D FE model is presented. Then, the dispersion characteristics and the FRFs are investigated using the 2.5D FE and the Timoshenko beam model of the rail to discuss some notable differences between them.

4.1. Experimental validation of the 2.5D FE model

The vibration behaviour obtained using the 2.5D FE rail model has been compared with measurements to ensure that the vibration used as input to the 2.5D BE model is representative for a railway track. These measurements were made on a track near Munich as part of the European Roll2Rail project [37]. To obtain the track decay rate (TDR) according to EN 15641 [38], the FRFs (driving point and transfer) were measured via impact testing. An accelerometer was fixed at a stationary receiver position on the rail using a magnetic mount, while the excitation was applied at different distances from the accelerometer. This procedure was replicated with the 2.5D FE model, but instead of a fixed receiver, the force was applied at a fixed position to calculate the FRFs at the identical distances using reciprocity.
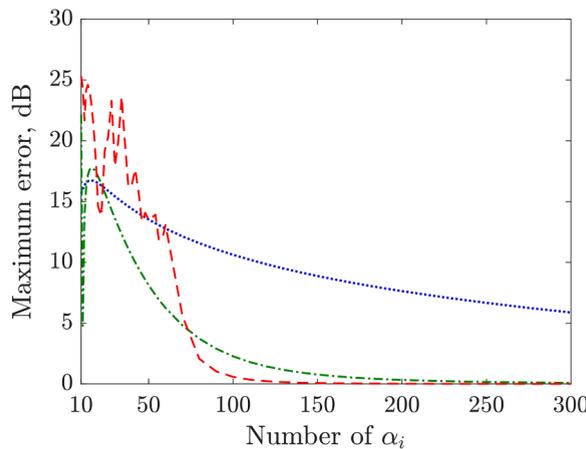

Fig. 6. Maximum error of the rail sound power using the 2.5D BE interpolation method in comparison with the classic 2.5D BE (re-assembly at each α, i.e. 55k computations), for increasing number of α_i points used in the pre-assembly and different interpolation order P; ▪▪▪, linear ($P = 1$); ▬·▬, quadratic ($P = 2$); ▬ ▬, quartic ($P = 4$).

The parameters used in the 2.5D FE rail model (and the Timoshenko beam model considered later) are listed in Table 1, along with the properties for the sleeper modelled as a Timoshenko beam. The cross-sectional area A and second moment of the area I of the rail were obtained numerically from the FE mesh, while the shear coefficients were taken from [11]. For the sleeper, the cross-section area A, and second moments of area I are geometric averages of values at the rail seat and centre to approximate the non-uniform sleeper cross-section as a uniform Timoshenko beam [30]. The density was adjusted to retain a mass of 280 kg for a sleeper length of 2.6 m.

To give a good fit of the 2.5D FE rail model with measurements, the parameters used in the simulations for the rail pad and ballast were adjusted based on the measured FRFs and TDR. The final parameters used are listed in Table 2. Measurements of the longitudinal FRFs were not available so the parameters are assumed identical to the lateral ones.

The calculated driving point mobilities in the vertical direction for a force applied at the top of the rail head centre, and in the lateral direction for a force applied at the centre of the rail head side, are compared with the corresponding measurements in Fig. 7. Overall, there is good agreement of the main trends in the magnitude and phase for both the vertical and lateral FRFs. In the vertical mobility, the two peaks around 80 and 300 Hz, are well captured. The first represents the resonance of the combined rail and sleeper mass on the ballast stiffness and the second is the rail-on-pad resonance [1]. This confirms that the vertical track support parameters were well estimated. Some peaks are missing in the predictions, e.g. the sharp peak around 1060 Hz in Fig. 7(a) corresponding to the vertical pinned-pinned resonance. This is a consequence of using the equivalent continuous support instead of discrete supports. In the lateral mobility there is a mismatch of the fundamental peak around 80 Hz in the measurement which is closer to 50 Hz in the predictions. The lateral mobility is constrained by the lateral and vertical support dynamics due to the rotation in the rail foot and the eccentricity of the support. Although the stiffness is distributed across the rail foot (as shown in Fig. 1) it is connected to a single point on the sleeper, which does not allow for coupling the sleeper rotation with the rail foot rotation appropriately. Increasing the vertical rail pad stiffness could lead to better agreement in the lateral mobility, while at the same time causing a disagreement in vertical mobility. In comparison to the model, the measured lateral mobility increases above 5 kHz. Additional measurements (not reported here) have confirmed that this is due to a resonance in the mounting of the accelerometer.

The corresponding vertical and lateral TDRs obtained from the model and the measurement are compared in Fig. 8. A close agreement can be seen in the vertical TDR over the whole frequency range. The lateral TDR agrees well between 100 Hz and 2.5 kHz. Below 100 Hz, the mismatch of the fundamental peak causes an underestimation of the measured TDR. Above 2.5 kHz the predicted lateral TDR is lower than the measurement.

Overall, the implemented 2.5D FE model of the rail shows a good agreement with measurements performed on a track. Remaining differences may be reduced by using a discretely supported track model. However, in this work a continuously supported track is preferred, as the support dynamics can be directly implemented in the EoM of the 2.5D FE model, allowing a more thorough analysis of the wave propagation in the supported rail.

4.2. Waves in the supported 2.5D FE and Timoshenko beam models

The dispersion curves of the supported rail (including the sleepers) were calculated using the 2.5D FE model and the Timoshenko beam models by solving for the free vibration via Eq. (6). A total number of 80 waves were extracted from the 2.5D FE calculations to ensure all propagating waves that are of interest are included. The wave solutions were ordered to allow them to be shown as continuous lines over frequency, using the wave assurance criterion, as defined by Houillon et al. in [39] for comparing the wave shapes between consecutive frequencies. The longitudinal wavenumbers κ_n of the ten waves that cut on below 10 kHz are shown in Fig. 9 in terms of their real part κ_{re}; they are plotted separately for symmetric waves I – V in which vibration is predominantly vertical/longitudinal, and antisymmetric waves i – v in which vibration is predominantly lateral. For comparison, the wavenumber k in air is added. The deformed shapes of the different wave types are illustrated in Fig. 10 at their cut-on frequency.

The vertical bending wave I, the longitudinal wave II, the lateral bending wave i, and the torsion wave ii are shown for all frequencies. At low frequencies, they correspond to waves in which the whole rail section vibrates rigidly. Due to the added support, small peaks or dips in wavenumber can be observed at frequencies below 300 Hz; they correspond to resonances of the rail on the support [1]. In the case of a dynamic support stiffness, the cut-on frequencies f_c of these four waves used in Fig. 10 were estimated from the frequency of the rail-on-pad resonance [1]. For clarity of presentation, the higher-order waves are only shown in Fig. 9 above their cut-on frequency, which is denoted by the vertical lines. For these waves, f_c was obtained more accurately by solving the linear EVP given in Eq. (5) for $\kappa = 0$. Three higher-order symmetric waves cut on below 10 kHz. Around 5.1 kHz, waves III and IV (foot flapping

Table 1

Parameters of the UIC60 rail and the sleeper.

Parameter	Units	Rail	Sleeper
Young's modulus	GPa	210	57
Poisson's ratio	—	0.3	0.2
Density	kg/m^3	7850	2400
Material loss factor	—	0.005	0.0083
Cross-section area	m^2	7.7×10^{-3}	4.5×10^{-2}
Second moment of the area (vertical)	m^4	30.3×10^{-5}	1.2×10^{-4}
Second moment of the area (lateral)	m^4	5.1×10^{-5}	2.2×10^{-4}
Shear coefficient (vertical)	—	0.393	0.83
Shear coefficient (lateral)	—	0.539	0.83

Table 2

Rail pad and ballast parameters obtained from measurements.

Parameter	Units	Vertical	Lateral/Longitudinal
Rail pad stiffness	MN/m	105	20
Rail pad loss factor	–	0.15	0.10
Ballast stiffness	MN/m	100	5
Ballast damping	kNs/m	50	150
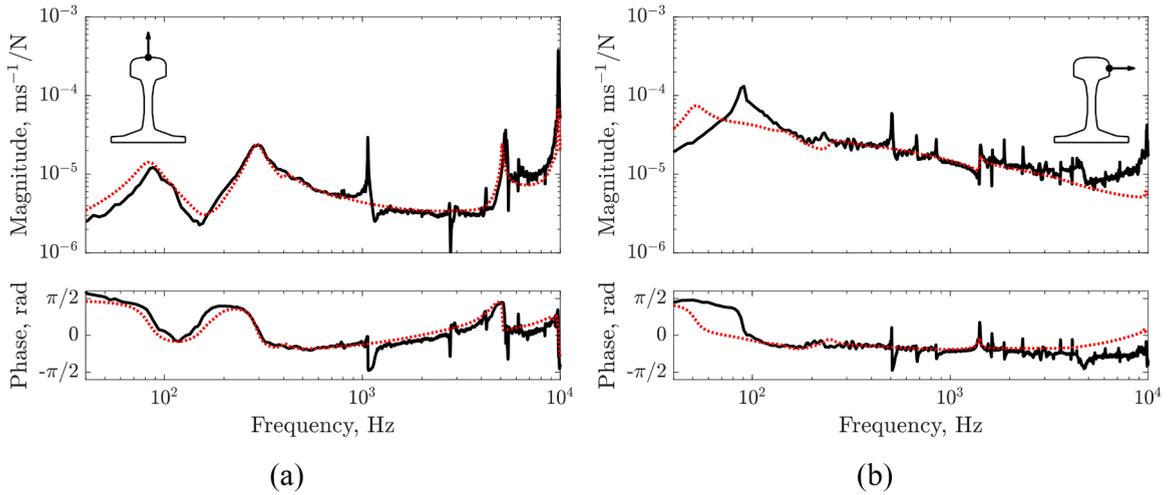
Fig. 7. Comparison of the driving point mobilities from the 2.5D FE model with measurements performed on a track in (a) vertical and (b) lateral direction; ▪ ▪ ▪, 2.5D FE model; ▬, measurement ([37]).
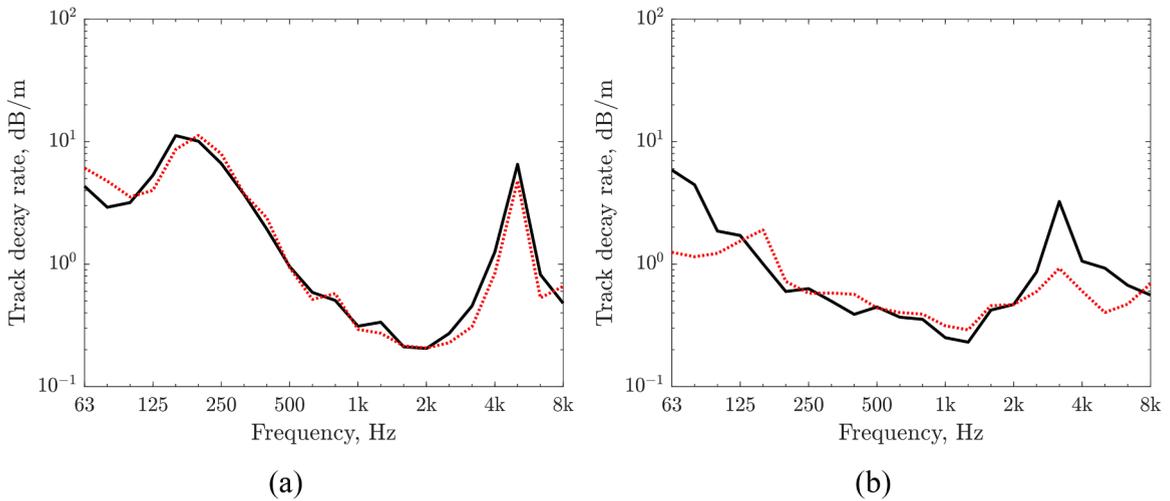
Fig. 8. Comparison of the track decay rates from the 2.5D FE model with measurements performed on a track in Munich in (a) vertical and (b) lateral direction; ▪ ▪ ▪, 2.5D FE rail; ▬, measurement ([37]).

and shear wave) and at 9.8 kHz wave V cut on. The higher-order antisymmetric waves iii – v (web bending waves) cut on around 1.4 kHz, 4.2 kHz, and 9.6 kHz, respectively.

Waves I and IV correspond to the two waves present in the Timoshenko beam model for vertical vibration. The vertical wave I is well captured below 4 kHz and the shear wave IV up to 10 kHz. The waves in the 2.5D FE model start coupling with other higher-order waves, which are not included in the classical Timoshenko beam model. The coupling of vibration occurs gradually when approaching the cut-on frequencies of higher-order waves, as can be seen in a change of slope of the corresponding wavenumbers. As an example, wave I includes foot flapping from around 2 – 3 kHz, see e.g. the illustrations in [14,40].

In the lateral direction, only the lateral bending wave exists as a propagating wave in the Timoshenko beam results below 10 kHz. It
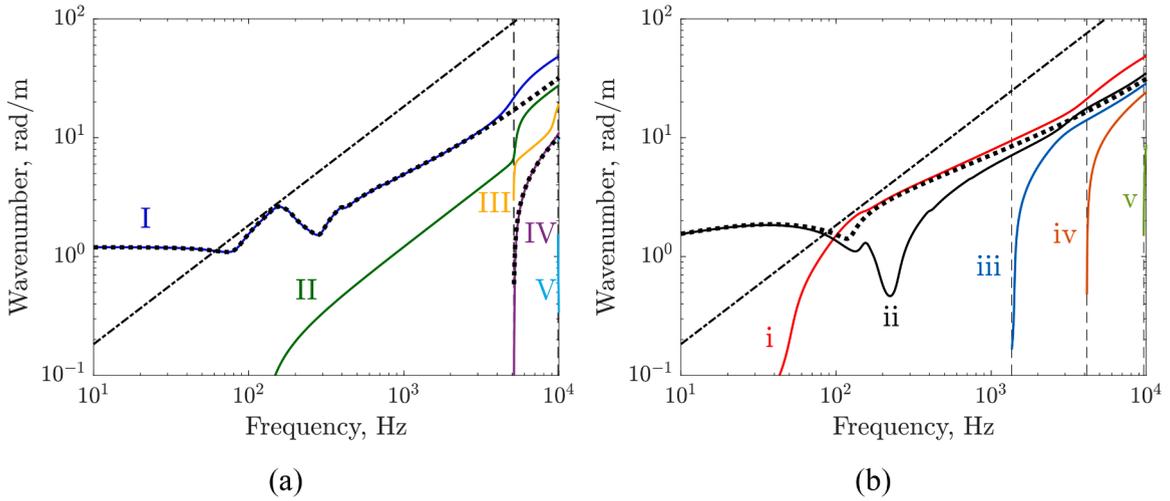
Fig. 9. Real part of the wavenumbers of the waves that propagate below 10 kHz separated between (a) symmetric waves I – V and (b) antisymmetric waves i – v; ▬, 2.5D FE rail; ▪▪▪, Timoshenko rail; — · —, wavenumber in air; — —, cut-on frequencies.
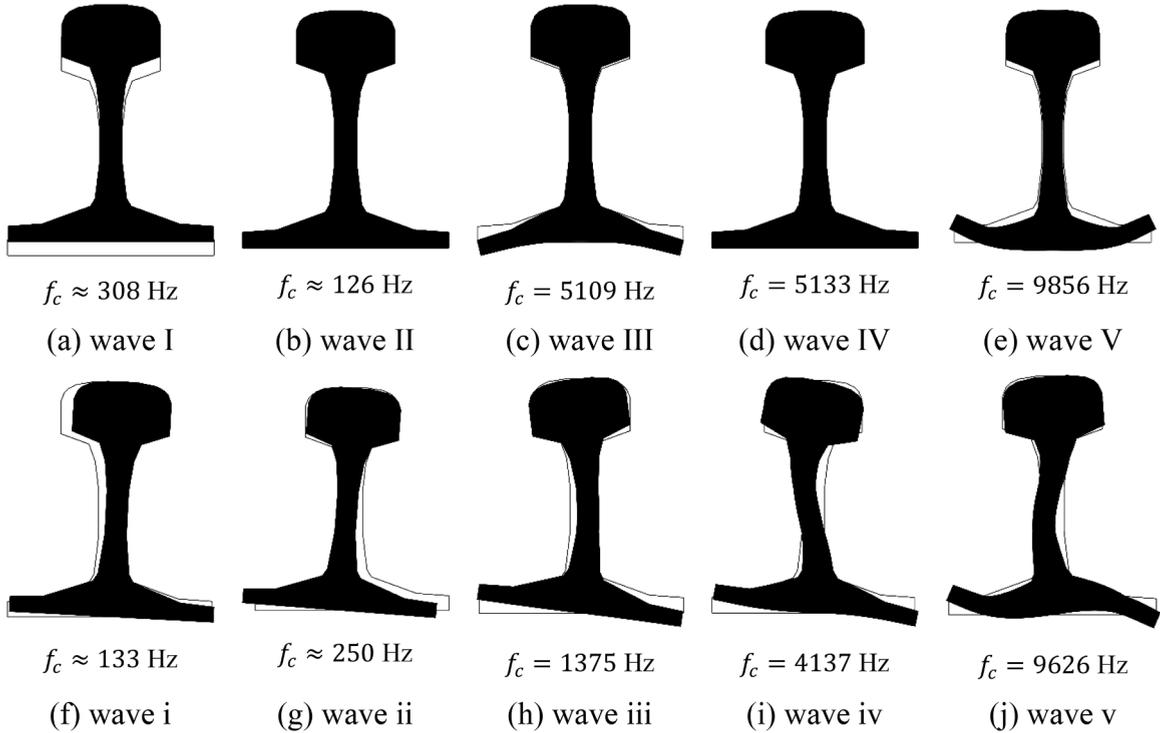

Fig. 10. Shapes of the symmetric waves I – V in (a) – (e) and the antisymmetric waves i – v in (f) – (j) at their cut-on frequency ($\kappa = 0$).

follows wave ii below 100 Hz and above 4 kHz, while between these frequencies it follows the trend of wave i. In the 2.5D FE model, the dynamic stiffness of the support is applied to the rail foot, i.e. with a vertical distance from the rail centroid, whereas in the Timoshenko beam model the stiffness is applied at the centroid. Thus, there is a mismatch in the lateral direction since there is no torsion or cross-section deformation in the Timoshenko beam model. In the vertical direction, where the stiffness is aligned with the rail centre, a good fit of both models can be seen.

The corresponding imaginary parts of the wavenumbers κ_{im} are plotted in Fig. 11 in terms of their decay rate $\Delta = -8.686\,\kappa_{\text{im}}$. Again, peaks and dips below 300 Hz are related to the track resonances and denote zones with lesser/stronger attenuation. The higher-order waves have high decay rates below their cut-on frequency, as they only exist as near-field waves, but they tend to a value between 0.1 and 10 dB/m after cutting on in the frequency range up to 10 kHz. The peaks in the decay rates around 400 Hz, 750 Hz and

1150 Hz, correspond to vertical sleeper resonances, which dissipate energy from the waves in the rail. As the rail foot rotation in the antisymmetric waves is constrained by the vertical stiffness of the support, the same peaks can be seen in symmetric and antisymmetric waves. Due to the low lateral pad stiffness, the lateral sleeper modes (longitudinal to the sleeper) do not appear.

The decay rate of the vertical bending wave in the Timoshenko beam model matches well with wave I below 2 kHz but underestimates it at higher frequencies. The vertical shear wave of the Timoshenko beam model matches well with wave IV. The lateral bending wave of the Timoshenko beam has a decay rate that follows wave ii below 100 Hz and follows wave i above this. From 3 kHz, it follows wave iii. The decay rate of the second wave in the Timoshenko beam is also shown, but it does not follow any of the depicted waves of the 2.5D FE model, as the corresponding wave cuts on only above 10 kHz.

4.3. Frequency response of the supported rail

The wave propagation characteristics of the waves that exist in a railway track have been observed. However, whether one of these waves is excited in the rail depends on the direction of the applied force, the location of the driving point on the rail and the location at which the vibration is observed.

4.3.1. Mobilities at the driving point

In Fig. 12 the rail point mobility for a vertical force applied to the centre of the rail head (N_1 in Fig. 1) is shown. The Timoshenko beam and the 2.5D FE model are compared with each other. For the latter, the magnitudes of the FRFs of the individual waves that cut on below 10 kHz are shown, as well as the sum over the first 80 waves. Only symmetric waves (I – V) contribute significantly to the vertical mobility for the vertical force applied at the rail head centre. There is good agreement between the two models up to 4 kHz, although first deviations occur from 1 kHz. This is due to the missing cross-section deformation and the higher-order waves.

By separating the wave solutions, the contribution of each wave in specific frequency regions can be observed. Waves I and IV dominate the driving point FRF at low frequencies. Wave IV is a near-field wave below 5 kHz. Above 3 kHz, the amplitude of wave I gradually reduces, as it is transformed from a vertical bending to a foot flapping wave, meaning there is less rail head vibration. Around 5.1 kHz, the cut-on of waves III and IV causes a strong peak in the vertical FRF, i.e. these two waves have a strong vertical component at the rail head in this frequency region. At higher frequencies, wave II dominates the vertical FRF, as it develops a strong vertical component in the rail head above 5 kHz, whereas waves III and IV become longitudinal in nature. The peak around 9.8 kHz is caused by the cut on of wave V.

Fig. 13 shows the vertical transfer mobility at the rail foot node (N_2 in Fig. 1) for a force applied at the rail head (N_1) at $x = 0$ in the 2.5D FE model. For comparison, the vertical mobility of the Timoshenko beam model is added. While the latter result is unchanged from Fig. 12, the 2.5D FE model has an increased vertical vibration, from about 1 kHz, compared with the driving point FRF in Fig. 12. This occurs because the contribution of the waves is slightly different compared with the rail head, i.e. waves I, II and V are more dominant between 1 and 5 kHz at the rail foot. Above 1 kHz, there also is a significant phase difference between the overall FRF and that in Fig. 12, i.e. at $x = 0$ the foot flapping motion is out-of-phase with the vertical vibration at the rail head over some frequency range. This may change over distance, as each wave has a different phase speed and decay rate.

The lateral driving point mobility for the force applied to the rail head centre at N_1 is shown in Fig. 14, including the solution for the Timoshenko beam and the 2.5D FE model, for which the overall FRF is again separated into the contribution per wave. For the lateral force, only antisymmetric waves contribute significantly to the overall FRF. There is a large difference between the two models over the whole frequency range. This is mainly because, in the 2.5D FE model, the force is applied with a vertical offset from the shear centre
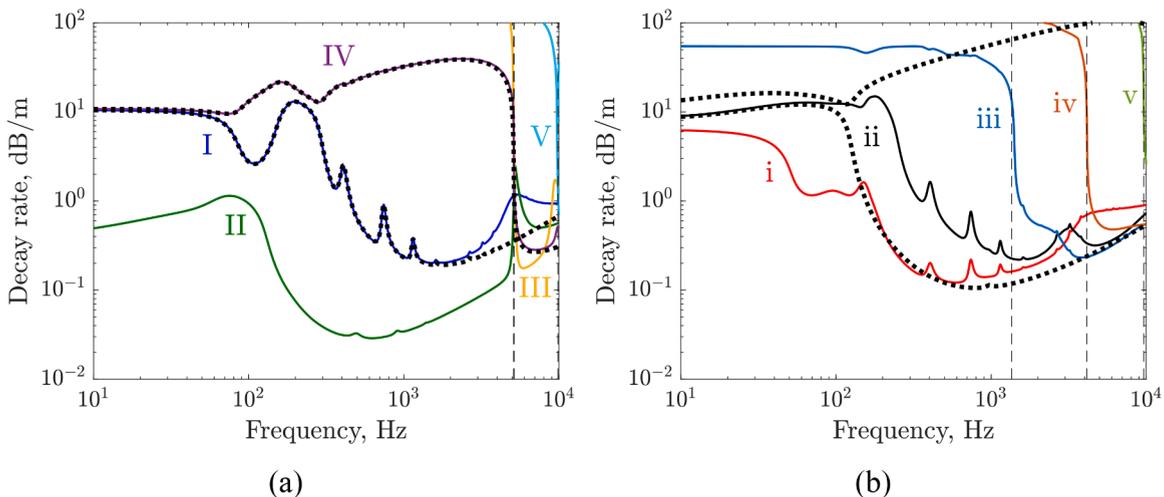

Fig. 11. Decay rates of the waves that become propagative below 10 kHz separated between (a) symmetric waves I – V and (b) antisymmetric waves i – v; ▬, 2.5D FE model; ▪ ▪, Timoshenko beam; — —, cut-on frequencies.
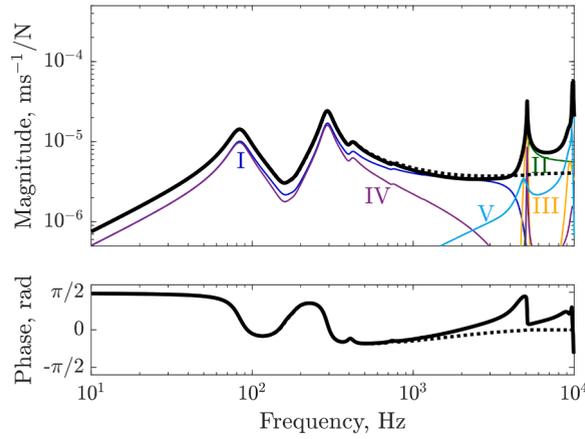
Fig. 12. Vertical rail driving point mobility at $x = 0$ for a vertical force applied to the rail head centre (N_1), separated between the different waves; ▬, 2.5D FE sum of all waves; —, 2.5D FE waves I – V; ▪ ▪ ▪, Timoshenko beam.
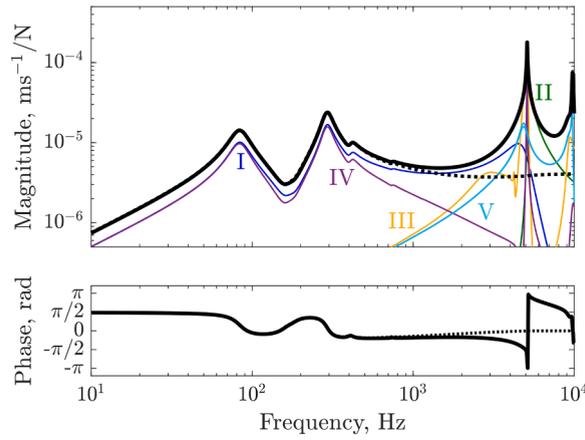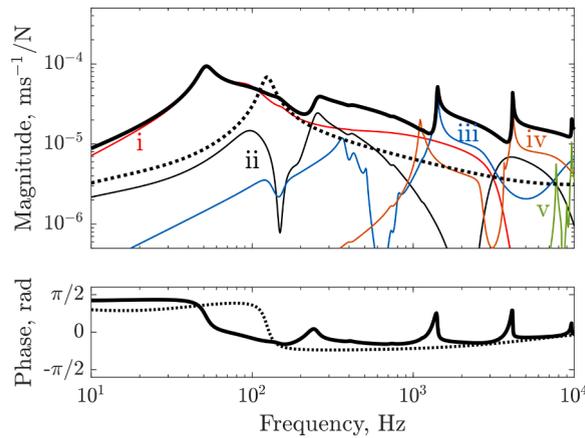

Fig. 13. Vertical rail mobility at the rail foot (N_2) at $x = 0$ for a vertical force applied to the rail head centre (N_1), separated between the different waves; ▬, 2.5D FE sum of all waves; —, 2.5D FE waves I – V; ▪ ▪ ▪, Timoshenko beam.

Fig. 14. Lateral rail driving point mobility at $x = 0$ for a lateral force applied to the rail head centre (N_1) separated between the different waves; ▬, 2.5D FE sum of all waves; —, 2.5D FE waves i – v; ▪ ▪ ▪, Timoshenko beam.

of the rail, which couples bending and torsion of the section; the foundation eccentricity also has an influence. In the lateral Timoshenko beam model, the force and foundation are assumed to be co-located with the shear centre and torsion is neglected. To correct for this, a semi-analytical rail model including torsion, as in [11], could be used. In the 2.5D FE model, wave i mostly dominates the FRF at frequencies below 1 kHz, with a contribution of wave ii around 200 – 700 Hz. Waves iii, iv and v produce peaks around 1.5 kHz, 4.3 kHz and 9.7 kHz, respectively, and each of these waves dominates the FRF above its cut-on frequency.

While the Timoshenko beam model can represent the vertical rail mobility at the driving point reasonably well up to about 4 kHz, in the lateral direction it is not a good approximation for the rail mobility.

4.3.2. Adjusting the decay rates of the Timoshenko beam

As seen from the driving point mobilities, depending on the force location and direction, only some of the waves are excited in the rail. Different waves can dominate the FRF in certain frequency regions, and given their different decay rates, it may also be different waves that dominate the FRF at a certain distance x. As the decay rates in the Timoshenko beam model are different from those from the 2.5D FE model in some frequency regions, see Fig. 11, the transfer FRFs over larger distances will be affected. Consequently, to isolate the effect of cross-section deformation on the radiated sound power, the differences in the wave decay rates should be taken into account, to ensure that differences in radiated noise are only due to the cross-section deformation.

For the vertical rail vibration, the decay rates of waves I and IV of the 2.5D FE model agree reasonably well with the corresponding waves in the Timoshenko model, see Fig. 11(a). The differences are equalised by adjusting the imaginary part of the wavenumber κ_{im} of the Timoshenko beam model to match those of the corresponding waves of the 2.5D FE model. Therefore, the propagating vertical bending wave in the Timoshenko beam model is assigned the imaginary part of wave I and the shear wave of the Timoshenko beam model, which is a near-field wave below 5.1 kHz, is given that of wave IV.

In Fig. 15, the vertical transfer mobility of the 2.5D FE model at position N_1 is compared with the Timoshenko beam model with the corrected wavenumbers over a distance of 25 m at the frequencies of 1 kHz and 5.1 kHz. For reference, the results from the Timoshenko beam with the original wavenumbers are added. At 1 kHz, the transfer mobility of all three models aligns well, as the original wavenumbers of the two models are almost identical. Within the distance of 25 m, the propagating wave I dominates the transfer FRF, while the near-field wave IV quickly decays away, as expected from their decay rates. At 5.1 kHz, a mismatch occurs if the original Timoshenko beam wavenumber is used. Thus, the radiated sound would be overestimated using the Timoshenko beam model. Adjusting the imaginary part of the wavenumber ensures a good match. Close to the driving point, wave III contributes to the FRF of the 2.5D FE model, which is why the Timoshenko beam result does not align well near $x = 0$. Due to interference between multiple waves in the 2.5D FE model, the transfer FRF shows oscillations about the average wave decay.

For the lateral vibration, from Fig. 11(b), it can be seen the decay rate of the bending wave from the Timoshenko beam envelopes the decay rates of waves i – iv that dominate the FRF in certain frequency regions. As there is a larger mismatch between the driving point FRFs of the two models in Fig. 14, a correction of the wavenumbers will not further improve the transfer FRFs and the original wavenumbers from the Timoshenko beam model are retained.

5. Effect of the rail cross-section deformation on the radiated sound

Using the wavenumber domain formulation, the rail vibration of the 2.5D FE and Timoshenko models can be obtained for a unit force applied at the rail head centre and used in the 2.5D BE model presented in Section 2.4 with the interpolation method from Section 3.2 to calculate the radiated sound power of the infinite rail. The results are then used to quantify the effect of the rail cross-section
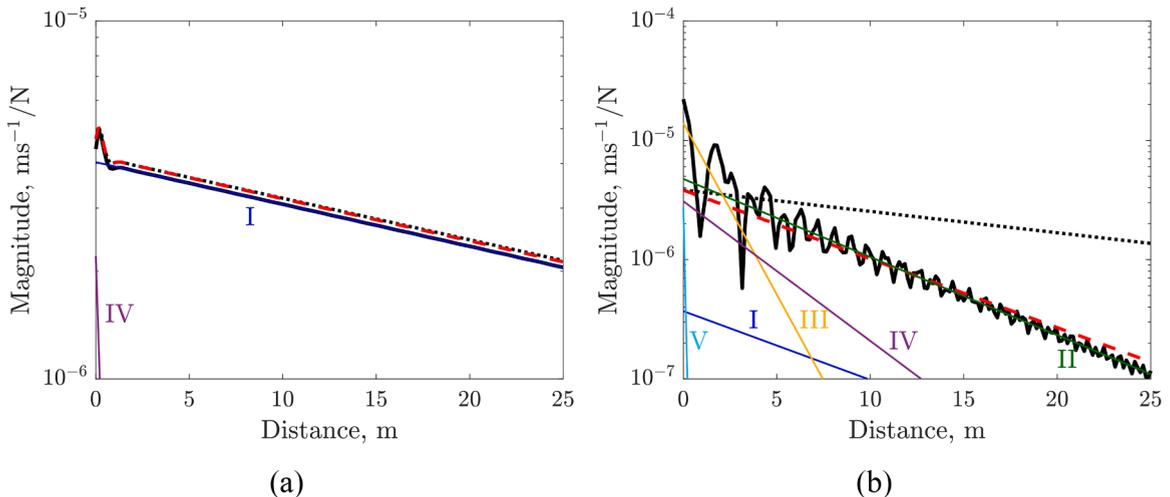

Fig. 15. Vertical transfer mobility over distance x for a vertical force applied to the rail head centre (N_1) at frequencies of (a) 1 kHz and (b) 5.1 kHz; ━, 2.5D FE model sum of all waves; —, 2.5D FE model waves I – V; ▪ ▪ ▪, Timoshenko beam; ━ ━, Timoshenko beam with corrected wavenumber.

deformation on the radiated sound power. For simplicity, in the 2.5D BE model, the effect of the ground is neglected and, in both cases, the rail is assumed to radiate sound into free space.

5.1. Radiated sound power

The sound power per unit squared force at the driving point N_1 on the rail head was calculated from the 2.5D FE and Timoshenko beam models in the frequency/wavenumber domain for 400 logarithmically spaced frequency points between 10 Hz and 10 kHz for vertical and lateral excitation. The results from the 2.5D FE model are shown in Fig. 16 in the frequency/wavenumber domain. Hence, these results are before performing the integration over wavenumber κ in Eq. (18). This highlights the contribution of different waves to the overall power. The wavenumber in air is also indicated, which denotes the limit of longitudinal wavenumber κ considered at each frequency, i.e. $\kappa < k$.

For the vertical excitation, the sound power maxima follow the dispersion curves of the symmetric waves I – V in Fig. 9(a). Below 60 Hz, only the vibrating near-fields contribute to the sound power, see also Fig. 9(a). Thus, the sound power is very low in this region. It remains low until 300 Hz, where the decay rate of wave I reduces. Between 300 Hz and 5 kHz, wave I radiates the most sound, but above 5 kHz its contribution diminishes and wave II becomes the dominant one [36], with a smaller contribution from the other waves.

For the lateral excitation, only antisymmetric waves i – v are contributing, which follow the dispersion curves shown in Fig. 9(b). Between 200 Hz and 1.4 kHz, wave i radiates most sound, with a lesser contribution from wave ii. Above 1.4 kHz, the higher-order waves cut on and different waves contribute in different frequency regions, so it is not as clear as for the vertical excitation which wave is the dominant one.

By evaluating the integral given in Eq. (18) over the perimeter Γ and wavenumber κ, the overall sound power per unit squared force from the 2.5D FE and Timoshenko models was obtained as a function of frequency. Fig. 17(a) compares the sound power from the 2.5D FE model to that from the Timoshenko beam model with and without adjusted wavenumbers for a vertical excitation, with the corresponding level differences shown in Fig. 17(b), where a positive value denotes an increase of the 2.5D FE model relative to the Timoshenko beam.

Below 3 kHz, the sound power of all three models is identical since vertical bending occurs with little or no cross-section deformation. The dips around 400, 700 and 1100 Hz are due to the increased decay rates at the vertical sleeper resonances. Above 3 kHz, the 2.5D FE rail has up to 15 dB higher sound power than the Timoshenko beam under vertical excitation. This increase is smaller if the Timoshenko beam wavenumbers remain uncorrected, since the original Timoshenko beam wave decay rates are lower than the 2.5D FE wave decay rate, see Fig. 11(a), which increases the effective vibrating length and thereby the sound power.

With the correction included, the effect of cross-section deformation can be addressed. Between 3 and 5 kHz, foot flapping increases the sound power by approximately 4 dB. In this frequency range, wave I transitions from vertical bending to foot flapping, while wave II has increased vertical rail head vibration. Around 5 kHz, the contributions of waves III and IV cause up to 13 dB increase. Wave V causes an increase of sound power by 15 dB at its cut-on frequency just below 10 kHz.

In Fig. 18, the sound power per unit squared force from the 2.5D FE model is compared with Timoshenko beam model for lateral excitation. In contrast to the vertical excitation, there are larger differences. Below 200 Hz, differences of up to 25 dB can be seen, due to the mismatch of the lateral track resonance and missing rail torsion. Between 200 Hz and 1.3 kHz the Timoshenko beam underestimates sound power by up to 3 dB, while above 1.5 kHz the average increase is about 8 dB. Above 1.3 kHz, wave iii contributes to the 2.5D FE rail vibration which increases sound power. Around 4.2 kHz wave iv cuts on leading to a peak in sound power with an increase of 17 dB.
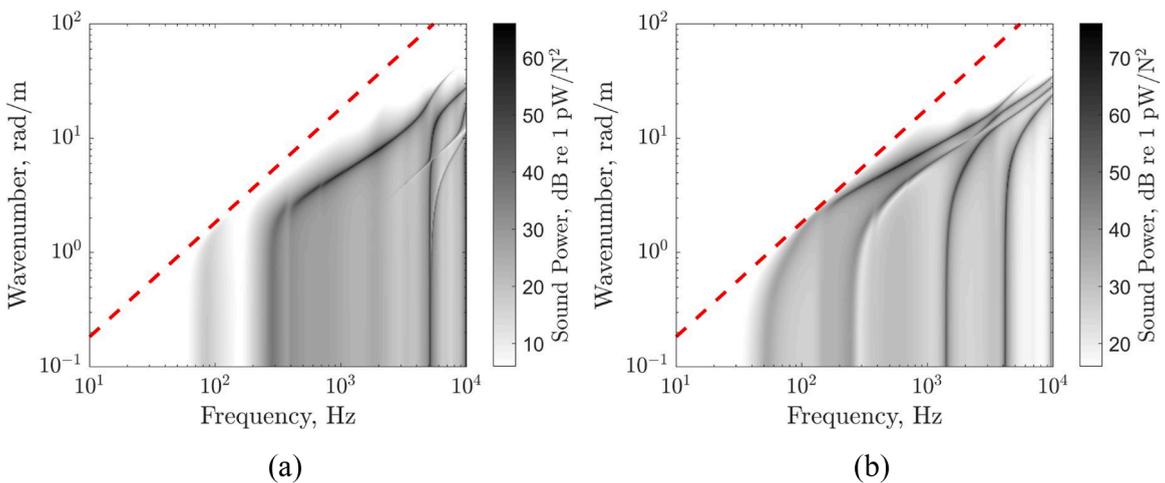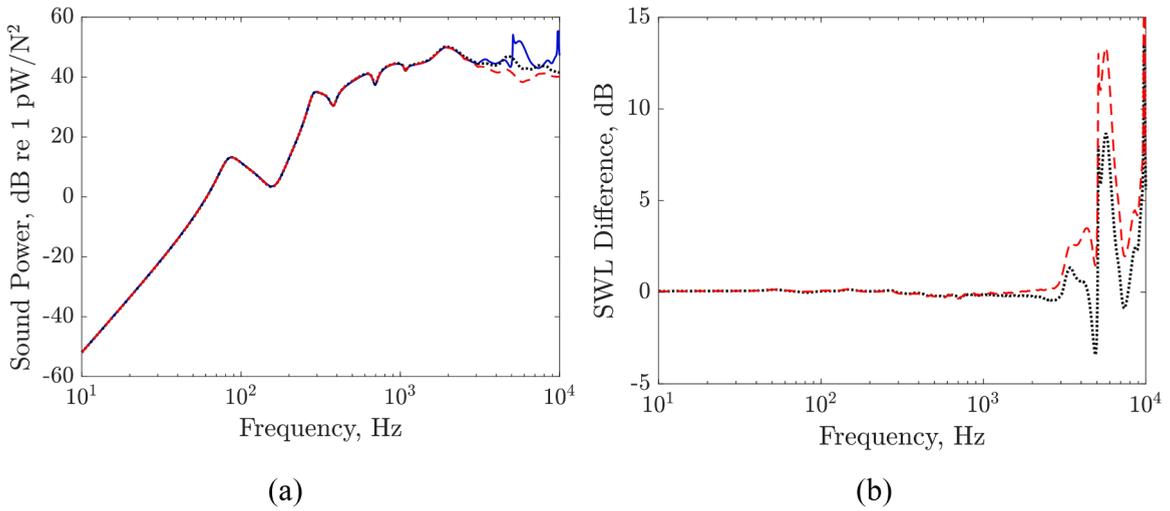

Fig. 16. Sound power level of the 2.5D FE rail per unit squared force applied to the rail head in (a) vertical and (b) lateral direction as a function of frequency and wavenumber; ▬ ▬, corresponding wavenumber in air.
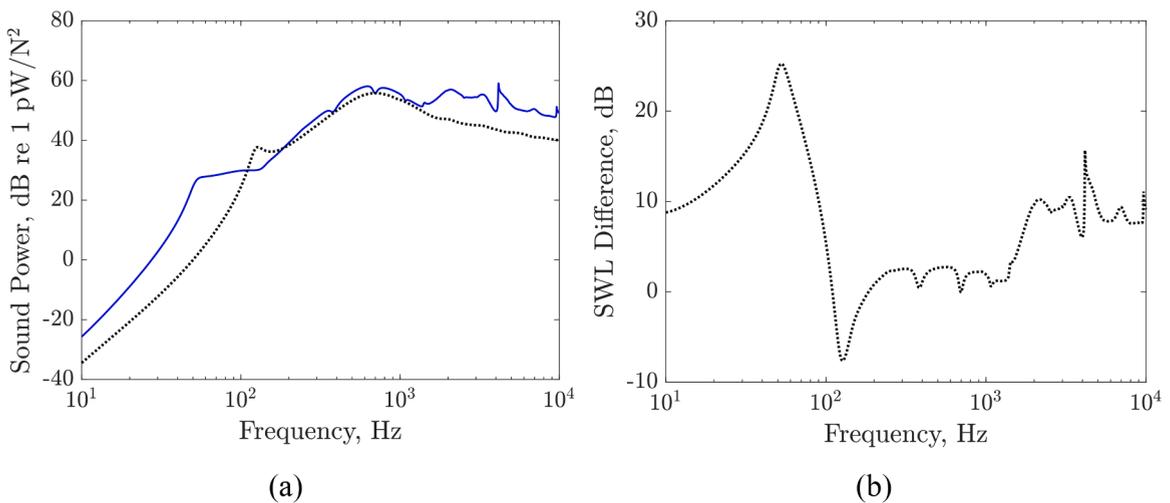
Fig. 17. (a) Sound power level per unit vertical squared force applied to the rail head at N_1 comparing the 2.5D FE and Timoshenko beam models; (b) level difference of sound power level per unit squared force of the Timoshenko beam models in comparison to the 2.5D FE model; ▪ ▪ ▪, Timoshenko beam; ━ ━; Timoshenko beam with corrected wavenumber; ━, 2.5D FE model.
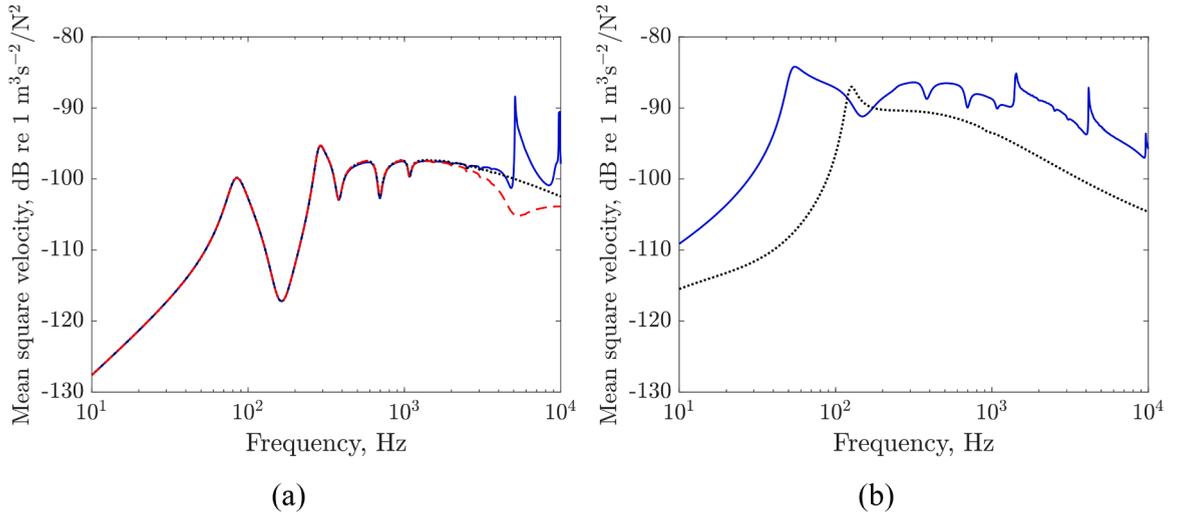
5.2. Spatially averaged mean square velocity

Calculating the normal velocity on the rail perimeter in the wavenumber domain and evaluating Eq. (19), the spatially averaged mean square velocity of the infinite rail was obtained. The results are shown in Fig. 19, including the 2.5D FE and Timoshenko beam rail models. For vertical excitation, results from the Timoshenko beam model both with and without corrected decay rates are shown. The results for vertical excitation show similar trends to the sound power in Fig. 17. Above 2 kHz, the results of the models start to diverge, and cross-section deformation leads to an increase in vibration per unit squared force. The lateral Timoshenko beam model shows larger differences relative to the 2.5D FE model, as already seen in Fig. 18 and explained above.

5.3. Radiation efficiency

From the spatially averaged mean square velocity and the radiated sound power, the radiation efficiencies of the rail radiating sound into free space were obtained from Eq. (20). Fig. 20 compares the radiation efficiency based on the vibration from the 2.5D FE model and from the Timoshenko beam model for vertical and lateral excitation at the rail head. The correction of the wavenumber has no effect on the radiation efficiency for the Timoshenko beam model, as both the sound power and the spatially averaged vibration are affected identically.

Fig. 18. (a) Sound power level per unit squared lateral force applied to the rail head at N_1 comparing the 2.5D FE and Timoshenko beam models; (b) level difference of sound power per unit squared force of the Timoshenko beam model in comparison to the 2.5D FE model; ━, 2.5D FE model; ▪ ▪ ▪, Timoshenko beam model.

Fig. 19. Spatially averaged mean square velocity per unit squared force applied in (a) vertical and (b) lateral direction to the rail head at N_1 comparing the 2.5D FE and Timoshenko beam models; ▪▪▪, Timoshenko beam; ▬ ▬; Timoshenko beam with corrected wavenumber; ▬, 2.5D FE model.

For vertical excitation, in Fig. 20(a), the radiation efficiency from both models is well aligned up to 3 kHz. Below the first resonance of the track on its foundation stiffness, around 80 Hz, the radiation efficiency increases by about 40 dB/decade ($\sim f^4$) which corresponds to a point dipole. Due to the support, wave propagation is highly attenuated below this frequency and the vibration is concentrated around the driving point, which leads to the point source-like behaviour [41]. Above 300 Hz, where the decay rate of the vertical wave I decreases, the increase with frequency tends to be closer to 30 dB/decade ($\sim f^3$) corresponding to the behaviour of a line dipole. As the wavelength in air becomes more comparable to the distance between the rail head and foot, the interaction of the sound field produced by the two vibrating components leads to a dip around 1 kHz and a peak around 2 kHz [42]. Above 3 kHz, differences between the two models can be seen since the different waves in the 2.5D FE rail model cause stronger interference if parts of the rail head and foot vibrate in- or out-of-phase. Thus, in comparison with the Timoshenko beam model there are more oscillations around 0 dB.

For lateral excitation, see Fig. 20(b), differences are present from lower frequencies. This is mainly due to the missing torsional motion of the rail and the mismatch of the resonances in the rail support, i.e. the peaks are not aligned, as shown e.g. in Fig. 14. However, the overall trend is still captured. Around 700 Hz, both curves reach a peak, and above 1 kHz, there are dips and peaks in the results from the 2.5D FE model due to the presence of the different waves, which do not occur in the Timoshenko beam results, which have a smoother radiation efficiency close to unity.

Although the radiation efficiencies suggest there are no large differences between the two models, in Section 5.1 it was shown that there are much larger differences in the radiated sound power due to the cross-section deformation.

6. Applying the 2.5D FE and Timoshenko beam models in rolling noise predictions

The results in the previous section were calculated for a unit squared force applied to the rail to study the sound radiation of the Timoshenko beam and 2.5D FE model. In this section, the rail models are included in a wheel/track interaction model for comparison of rail sound power with and without cross-section deformation in a full rolling noise prediction scheme based on the TWINS approach [6]. Results are calculated for a roughness corresponding to the TSI limit given in [43], including the contact filter effect [1].

The multi-DoF wheel/track interaction, including the vertical ($i = z$) and the lateral ($i = y$) DoFs is solved in the frequency domain, giving the contact forces $\mathbf{f}_c$ as [44]

$$\mathbf{f}_c = \begin{Bmatrix} f_{c,y} \\ f_{c,z} \end{Bmatrix} = [\mathbf{Y}_r + \mathbf{Y}_w + \mathbf{Y}_c]^{-1} \begin{Bmatrix} 0 \\ i\omega R \end{Bmatrix} \tag{23}$$

where $\mathbf{Y}_r$, $\mathbf{Y}_w$, $\mathbf{Y}_c$ are the 2×2 mobility matrices of the wheelset, rail and contact zone, comprising lateral and vertical driving point mobilities Y_y and Y_z, respectively, as well as the vertical-lateral cross mobilities $Y_{yz} = Y_{zy}$, and R is the magnitude of roughness in the vertical direction. The rail mobilities in $\mathbf{Y}_r$ are based on the models presented in this paper (see Fig. 12 and Fig. 14), while the wheel mobilities $\mathbf{Y}_w$ are calculated from the rotating wheelset model developed by the authors in [45], and the contact zone mobilities $\mathbf{Y}_c$, including coupling through the contact spring and creep forces, are calculated according to Thompson [46].

From the transfer functions W_i^{unit} of rail sound power per unit squared force applied to the rail head in the i-th direction (see Fig. 17 and Fig. 18) and the corresponding contact force components $f_{c,i}$ from Eq. (23), the total rail sound power is summed over the $M = 2$ components W_i as
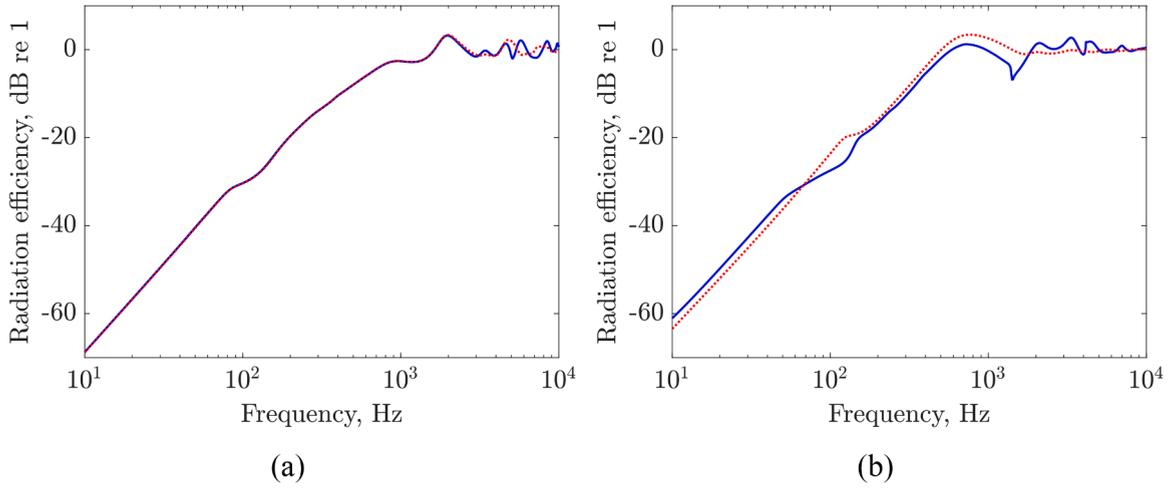
Fig. 20. Radiation efficiency of the rail for (a) vertical and (b) lateral excitation, comparing the two different models; ▬, 2.5D FE; ▪▪▪, Timoshenko.
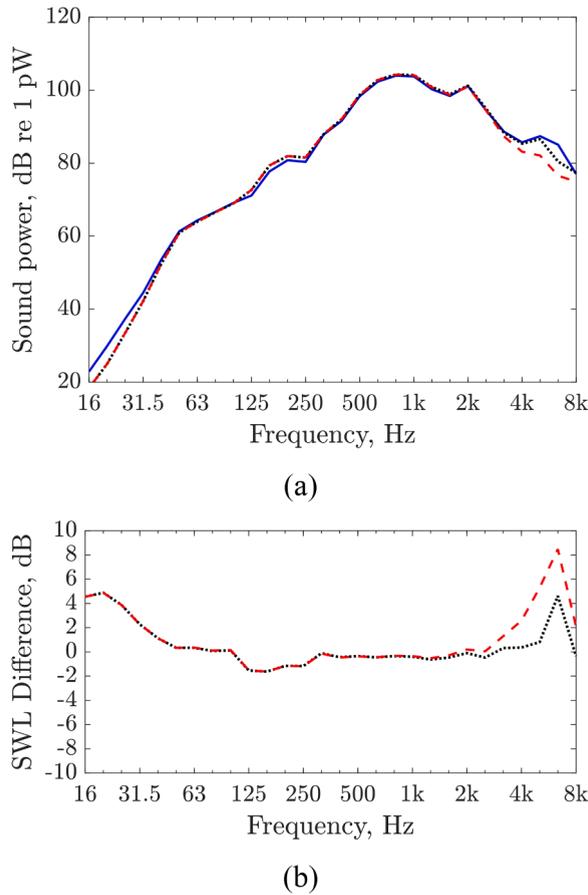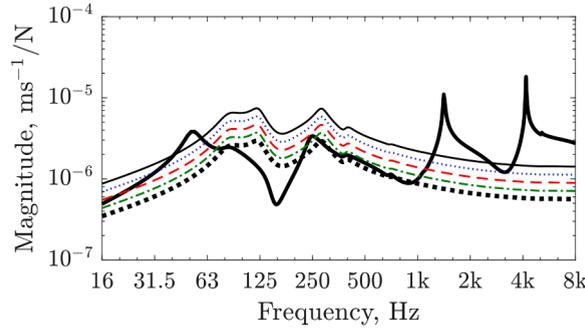

Fig. 21. Comparison of rail sound power in rolling noise predictions using different models in terms of (a) absolute levels and (b) relative differences; ▪▪▪, Timoshenko beam; ▬ ▬, Timoshenko beam with corrected wavenumber; ▬, 2.5D FE model.

Fig. 22. Vertical/lateral mobility cross-term Y_{yz} of the rail comparing the 2.5D FE rail with 10 mm offset of the excitation (━) with the Timoshenko beam rail using different correction factors X_{dB}: ━, −8 dB; ▪▪▪, −10 dB; ▬ ▬, −12 dB; ▬ ▪ ▬, −14 dB; ▪ ▪ ▪, −16 dB.

$$W = \sum_{i}^{M} W_i = \sum_{i}^{M} W_i^{\text{unit}} |f_{c,i}|^2. \tag{24}$$

By employing the 2.5D FE and the Timoshenko beam rail models (the latter with or without corrected decay rates) in the rolling noise model, the effect of cross-section deformation on the rolling noise is calculated. The results of rail sound power are shown in Fig. 21, including relative differences, where a positive value denotes an underestimation in comparison with the 2.5D FE model. Differences of up to 5 dB occur below 315 Hz, due to differences in the track resonances in the Timoshenko beam model. Up to 2.5 kHz, the results are almost equal, but above this the Timoshenko beam models diverge from the 2.5D FE model, causing an underestimation of up to 8 dB due to the missing cross-section deformation. Using the original wave decay rates in the Timoshenko beam, the underestimation is reduced to 4-5 dB, since the decay rates are lower at higher frequencies.

The above calculations assumed the wheel/rail contact position on the rail is at the rail head centre (see N_1 in Fig. 1), which induces no vertical/lateral coupling via rail torsion. In TWINS, the vertical/lateral rail cross mobility is approximated as a weighted average of the vertical (Y_z) and lateral (Y_y) Timoshenko beam mobilities as [47]

$$Y_{yz} = Y_{zy} = 10^{X_{dB}/20} \sqrt{Y_y \cdot Y_z} \tag{25}$$

where X_{dB} is an empirical correction factor that scales the cross mobility.

The calculations were repeated with a lateral offset of 10 mm of the contact position from the rail head centre. In the 2.5D FE model, this offset can be directly implemented by shifting the excitation position, while for the Timoshenko beam model, different values of X_{dB} between −8 dB and −16 dB were used. The vertical/lateral rail cross mobility is shown in Fig. 22. The coupling induced in the Timoshenko beam rail via Eq. (25) can approximate the 2.5D FE rail only in a limited frequency region, depending on the value of X_{dB}. At frequencies above 1 kHz, the approximation is inaccurate due to the missing higher-order waves seen as peaks in the 2.5D FE rail.

Due to the additional vertical/lateral coupling in the rail contact mobility, the contact forces from the wheel/track interaction change, and consequently also the rail vibration response and its radiated sound power. For the 2.5D FE rail, another 2.5D BE calculation was required to obtain new transfer functions W_i^{unit} with the offset due to the added torsion. The difference in the rail sound power between the 2.5D FE and the Timoshenko rail (original wavenumbers) for the same values of X_{dB} is shown in Fig. 23, including the case where $Y_{yz} = 0$ (as in Fig. 21). Results are separated between the power W_y and W_z for lateral and vertical rail excitation and total sound power W. A positive value denotes an underestimation of the 2.5D FE rail. Again, the correction may only improve the difference of the sound power in a limited frequency range, depending on the value of X_{dB}. For vertical excitation, results differ by up to 6 dB and are generally close to the case of $Y_{yz} = 0$. For lateral excitation, the differences are largest and reach 25 dB, similar to the transfer functions in Fig. 18, and the added coupling Y_{yz} does not approximate rail torsion well at low frequencies. Since the vertical excitation is dominating large parts of the spectrum, the maximum difference in overall rail sound power is reduced to about 8 dB. From above 1 kHz, the overall sound power tends to be identical to the case where vertical/lateral coupling is neglected ($Y_{yz} = 0$) and the missing cross-section deformation leads to an underestimation of the rail sound power of up to 5 dB in one-third octave bands.

Above about 2 kHz, the wheel dominates the sound power of rolling noise [1]. However, depending on the track parameters, the rail sound power at higher frequencies can be more significant when using the 2.5D FE rail than with the Timoshenko beam rail, especially for a soft rail pad.

7. Conclusions

For accurate high frequency rolling noise predictions, it is important to use a track model that adequately represents the rail vibration and the consequent sound radiation. Simpler rail models based on a Timoshenko beam neglect the effects of the rail torsion and cross-section deformation. A vibroacoustic model of a supported rail was implemented based on the 2.5D FE and BE approach. This uses an equivalent continuous support with a flexible sleeper and accounts for cross-section deformation of the rail and the sleeper
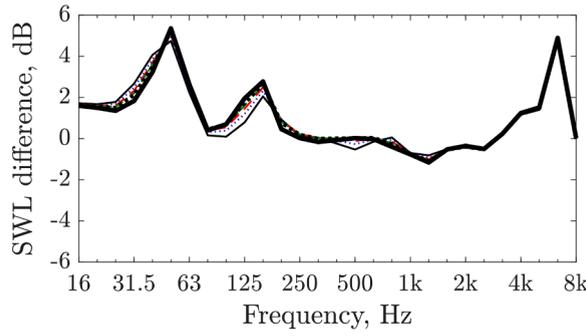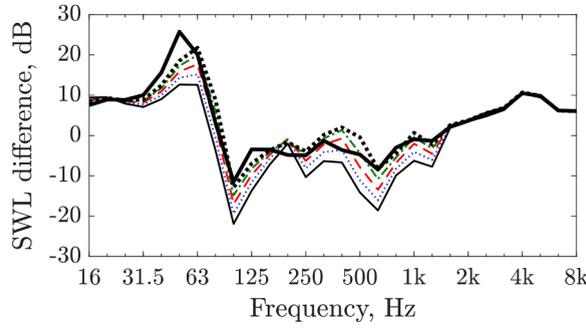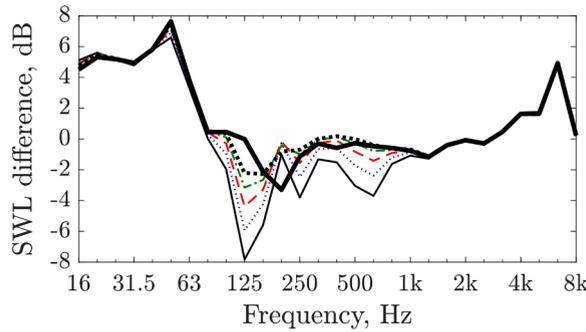
Fig. 23. Difference of rail sound power in rolling noise predictions for (a) vertical excitation W_z, (b) lateral excitation W_y, and (c) combined sound power W, comparing the 2.5D FE rail with off-centre excitation (10 mm offset) with a Timoshenko beam rail using correction factors X_{dB} to approximate Y_{yz} : —, −8 dB; ·· ·, −10 dB; ▬ ▬, −12 dB; ▬ · ▬, −14 dB; · · ·, −16 dB; ▬, $Y_{yz} = 0$.

flexibility. A novel interpolation method that interpolates the element coefficient vectors used to determine the system matrices of the 2.5D BE model has been developed. This approach significantly reduces the computational time for sound radiation calculations by avoiding the re-assembly of the fully populated matrices required in the classical approach.

The rail vibration obtained from the 2.5D FE model was compared with measurements showing good agreement and confirming the rail vibration input in the 2.5D BE model is representative. While the Timoshenko beam model only contains two waves for each direction, in the 2.5D FE model up to ten waves cut on below 10 kHz. The vertical bending and shear waves of the Timoshenko beam were clearly identified with waves in the 2.5D FE model, showing very similar dispersion characteristics, whereas in the lateral direction the correspondence was not as good. In the driving point mobilities, peaks produced by the higher-order waves are missing in the Timoshenko beam results. While there is good agreement between the vertical mobility of both models below 4 kHz, a larger difference occurs in the lateral mobility. From the wave decay rates and the transfer mobilities it could be seen that rail vibration decays differently over distance in the two models. To avoid the influence of this difference on the radiated sound, the wave decay of the Timoshenko beam was adjusted to match that of the 2.5D model.

For a vertical unit force applied to the rail head, the Timoshenko beam and 2.5D FE models radiate sound equally below 3 kHz. At

frequencies around 3 – 4 kHz, where foot flapping starts occurring, and above 5 kHz, where several waves are cut-on, the Timoshenko beam model underestimates the sound power; differences of up to 15 dB occur around 5 – 6 kHz. If the wave decay rates are not adjusted, the underestimation is smaller. For lateral excitation by a unit force, larger differences in sound power occur over the whole frequency range, as the Timoshenko beam is not a good representation of the rail vibration. Below 200 Hz, differences of up to 25 dB occur due to the mismatch of the track resonance from the missing rail torsion and foundation eccentricity, while above 1 kHz an underestimation of up to 15 dB is possible since the higher-order waves with cross-section deformation are not included.

Finally, the 2.5D FE and Timoshenko beam rail models were coupled in a rolling noise prediction scheme that follows the TWINS approach using the transfer functions of sound power per unit squared force. The results demonstrate that the Timoshenko beam underestimates the rail noise by 4 – 5 dB at frequencies above 2.5 kHz in one-third octave band resolution, due to the missing cross-section deformation. For an offset excitation, the missing rail torsion in the Timoshenko beam further reduces the accuracy. Whether this increase changes the overall sound power depends on the track parameters. Thus, in general the 2.5D FE model provides a better representation of the rail sound power.

CRediT authorship contribution statement

Christopher Knuth: Writing – original draft, Visualization, Validation, Software, Methodology, Investigation, Formal analysis, Conceptualization. **Giacomo Squicciarini:** Writing – review & editing, Supervision, Project administration, Methodology, Investigation, Conceptualization. **David Thompson:** Writing – review & editing, Supervision, Methodology, Investigation, Conceptualization.

Declaration of competing interest

The authors declare that they have no known competing financial interests or personal relationships that could have appeared to influence the work reported in this paper.

Acknowledgements

Data availability

Data is available in the University of Southampton online repository at https://doi.org/10.5258/soton/D3586.

References

[1] D.J. Thompson, Railway noise and vibration: mechanisms, modelling and means of control, Elsevier, Amsterdam, 2024 second ed.
[2] J.S. Theyssen, Towards time-domain modelling of wheel/rail noise: effect of the dynamic track model, Proceedings of the Institution of Mechanical Engineers, Part F: Journal of Rail and Rapid Transit 238 (4) (2024) 350–359, https://doi.org/10.1177/09544097231179514.
[3] R. Pieren, F. Georgiou, G. Squicciarini, D.J. Thompson (2022) Auralisation of combined mitigation measures in railway pass-by noise, InterNoise. Glasgow 21–24 August, INTER-NOISE and NOISE-CON Congress and Conference Proceedings, p1093–1101. https://doi.org/10.3397/IN_2022_0151.
[4] K.L. Knothe, S.L. Grassie, Modelling of railway track and vehicle/track interaction at high frequencies, Vehicle System Dynamics 22 (3–4) (1993) 209–262, https://doi.org/10.1080/00423119308969027.
[5] S.L. Grassie, R.W. Gregory, D. Harrison, K.L. Johnson, The dynamic response of railway track to high frequency vertical excitation, Journal of Mechanical Engineering Science 24 (2) (1982) 77–90, https://doi.org/10.1243/jmes_jour_1982_024_016_02.
[6] D.J. Thompson, B. Hemsworth, N. Vincent, Experimental validation of the TWINS prediction program for rolling noise, part 1: description of the model and method, Journal of Sound and Vibration 193 (1) (1996) 123–135, https://doi.org/10.1006/jsvi.1996.0252.
[7] D.J. Thompson, P. Fodiman, H. Mahé, Experimental validation of the TWINS prediction program for rolling noise, part 2: results, Journal of Sound and Vibration 193 (1) (1996) 137–147, https://doi.org/10.1006/jsvi.1996.0253.
[8] D.J. Thompson, M.H.A. Janssens, F.G. de Beer, TWINS Track-Wheel Interaction Noise Software, Theoretical manual (version 3.0), TNO-Report HAG-RPT-9900211, 1999.
[9] T.X. Wu, D.J. Thompson, Application of a multiple-beam model for lateral vibration analysis of a discretely supported rail at high frequencies, The Journal of the Acoustical Society of America 108 (3) (2000) 1341–1344, https://doi.org/10.1121/1.1285920.
[10] T.X. Wu, D.J. Thompson, A double Timoshenko beam model for vertical vibration analysis of railway track at high frequencies, Journal of Sound and Vibration 224 (2) (1999) 329–348, https://doi.org/10.1006/jsvi.1999.2171.
[11] D. Kostovasilis, D.J. Thompson, M.F.M. Hussein, A semi-analytical beam model for the vibration of railway tracks, Journal of Sound and Vibration 393 (2017) 321–337, https://doi.org/10.1016/j.jsv.2016.12.033.
[12] J.C.O. Nielsen, A. Igeland, Vertical dynamic interaction between train and track - influence of wheel and track imperfections, Journal of Sound and Vibration 187 (5) (1995) 825–839, https://doi.org/10.1006/jsvi.1995.0566.
[13] J. Yang, D.J. Thompson, A non-reflecting boundary for use in a finite element beam model of a railway track, Journal of Sound and Vibration 337 (2015) 199–217, https://doi.org/10.1016/j.jsv.2014.10.037.
[14] D.J. Thompson, Wheel-rail noise generation, part III: rail vibration, Journal of Sound and Vibration 161 (3) (1993) 421–446, https://doi.org/10.1006/jsvi.1993.1084.
[15] D.J. Mead, A general theory of harmonic wave propagation in linear periodic systems with multiple coupling, Journal of Sound and Vibration 27 (2) (1973) 235–260, https://doi.org/10.1016/0022-460X(73)90064-3.
[16] B.R. Mace, D. Duhamel, M.J. Brennan, L. Hinke, Finite element prediction of wave motion in structural waveguides, The Journal of the Acoustical Society of America 117 (5) (2005) 2835–2843, https://doi.org/10.1121/1.1887126.

[17] L. Gavrić, Computation of propagative waves in free rail using a finite element technique, Journal of Sound and Vibration 185 (3) (1995) 531–543, https://doi.org/10.1006/jsvi.1995.0398.

[18] L. Gry, Dynamic modelling of railway track based on wave propagation, Journal of Sound and Vibration 195 (3) (1996) 477–505, https://doi.org/10.1006/jsvi.1996.0438.

[19] C.-M. Nilsson, C.J.C. Jones, D.J. Thompson, J. Ryue, A waveguide finite element and boundary element approach to calculating the sound radiated by railway and tram rails, Journal of Sound and Vibration 321 (3–5) (2009) 813–836, https://doi.org/10.1016/j.jsv.2008.10.027.

[20] I. Bartoli, A. Marzani, F. Lanza di Scalea, E. Viola, Modeling wave propagation in damped waveguides of arbitrary cross-section, Journal of Sound and Vibration 295 (3–5) (2006) 685–707, https://doi.org/10.1016/j.jsv.2006.01.021.

[21] J. Ryue, S. Jang, D.J. Thompson, A wavenumber domain numerical analysis of rail noise including the surface impedance of the ground, Journal of Sound and Vibration 432 (2019) 173–191, https://doi.org/10.1016/j.jsv.2018.06.032.

[22] X. Zhang, D.J. Thompson, Q. Li, D. Kostovasilis, M.G.R. Toward, G. Squicciarini, J. Ryue, A model of a discretely supported railway track based on a 2.5D finite element approach, Journal of Sound and Vibration 438 (2019) 153–174, https://doi.org/10.1016/j.jsv.2018.09.026.

[23] W. Sun, D.J. Thompson, M.G.R. Toward, Z. Zeng, Modelling of vibration and noise behaviour of embedded tram tracks using a wavenumber domain method, Journal of Sound and Vibration 481 (2020) 115446, https://doi.org/10.1016/j.jsv.2020.115446.

[24] J.S. Theyssen, E. Aggestam, S. Zhu, J.C.O. Nielsen, A. Pieringer, W. Kropp, W. Zhai, Calibration and validation of the dynamic response of two slab track models using data from a full-scale test rig, Engineering Structures 234 (2021) 111980, https://doi.org/10.1016/j.engstruct.2021.111980.

[25] J.S. Theyssen, A. Pieringer, W. Kropp, Efficient calculation of the three-dimensional sound pressure field around a slab track, Acta Acustica 8 (2024) 4, https://doi.org/10.1051/aacus/2023068.

[26] D.J. Thompson, D. Zhao, G. Squicciarini, Simplified prediction models for acoustic installation effects of train-mounted equipment, Railway Engineering Science 32 (2024) 125–143, https://doi.org/10.1007/s40534-024-00333-9.

[27] M. Petyt, Introduction to finite element vibration analysis, Cambridge University Press, Cambridge, 2010 second ed.

[28] C.-M. Nilsson, S. Finnveden, Input power to waveguides calculated by a finite element method, Journal of Sound and Vibration 305 (4–5) (2007) 641–658, https://doi.org/10.1016/j.jsv.2007.04.025.

[29] V. Damljanović, R.L. Weaver, Forced response of a cylindrical waveguide with simulation of the wavenumber extraction problem, The Journal of the Acoustical Society of America 115 (4) (2004) 1582–1591, https://doi.org/10.1121/1.1675818.

[30] D. Kostovasilis, Analytical modelling of the vibration of railway track, University of Southampton, 2017. Ph.D. thesis.

[31] X. Zhang, D.J. Thompson, H. Jeong, M.G.R. Toward, D. Herron, C.J.C. Jones, N. Vincent, Measurements of the high frequency dynamic stiffness of railway ballast and subgrade, Journal of Sound and Vibration 468 (2020) 115081, https://doi.org/10.1016/j.jsv.2019.115081.

[32] L. Cremer, M. Heckl, B.A.T. Petersson, Structure-borne sound: structural vibrations and sound radiation at audio frequencies, Springer, Berlin, 2005 third ed.

[33] C.-M. Nilsson, C.J.C. Jones, Theory manual for WANDS 2.1 wave number domain FE-BE Software for structures and fluids, ISVR Technical Memorandum 975 (2007). No.

[34] T.W. Wu, Boundary element acoustics: fundamentals and computer codes, WIT Press, Ashurst, 2000.

[35] H.A. Schenck, Improved integral formulation for acoustic radiation problems, The Journal of the Acoustical Society of America 44 (1) (1968) 41–58, https://doi.org/10.1121/1.1911085.

[36] J.S. Theyssen, Simulating rolling noise on ballasted and slab tracks: vibration, radiation, and pass-by signals, Chalmers University of Technology, 2022. Ph.D. thesis.

[37] D.J. Thompson, G. Squicciarini, J. Zhang, I.Lopez Arteaga, E. Zea, M.G. Dittrich, E. Jansen, K. Arcas, E. Cierco, F.X. Magrans, A. Malkoun, E. Iturritxa, A. Guiral, M. Stangl, G. Schleinzer, B.Martin Lopez, C. Chafour, J. Wändell, Assessment of measurement-based methods for separating wheel and track contributions to railway rolling noise, Applied Acoustics 140 (2018) 48–62, https://doi.org/10.1016/j.apacoust.2018.05.012.

[38] EN 15461:2008 Railway applications – Noise emission – Characterisation of the dynamic properties of track sections for pass by noise measurements, European Committee for Standardization.

[39] L. Houillon, M.N. Ichchou, L. Jezequel, Wave motion in thin-walled structures, Journal of Sound and Vibration 281 (3–5) (2005) 483–507, https://doi.org/10.1016/j.jsv.2004.01.020.

[40] D.J. Thompson, Experimental analysis of wave propagation in railway tracks, Journal of Sound and Vibration 203 (5) (1997) 867–888, https://doi.org/10.1006/jsvi.1997.0903.

[41] D.J. Thompson, C.J.C. Jones, N. Turner, Investigation into the validity of two-dimensional models for sound radiation from waves in rails, The Journal of the Acoustical Society of America 113 (4) (2003) 1965–1974, https://doi.org/10.1121/1.1555612.

[42] X. Zhang, G. Squicciarini, D.J. Thompson, Sound radiation of a railway rail in close proximity to the ground, Journal of Sound and Vibration 362 (2016) 111–124, https://doi.org/10.1016/j.jsv.2015.10.006.

[43] ISO 3095, Acoustics – Railway applications – Measurement of noise emitted by rail-bound vehicles, International Organisation for Standardization, 2013.

[44] D.J. Thompson, Wheel-rail noise generation, part I: introduction and interaction model, Journal of Sound and Vibration 161 (3) (1993) 387–400, https://doi.org/10.1006/jsvi.1993.1082.

[45] C. Knuth, G. Squicciarini, D.J. Thompson, L. Baeza, Effects of rotation on the rolling noise radiated by wheelsets in high-speed railways, Journal of Sound and Vibration 572 (2024) 118180, https://doi.org/10.1016/j.jsv.2023.118180.

[46] D.J. Thompson, Wheel-rail noise generation, part IV: contact zone and results, Journal of Sound and Vibration 161 (3) (1993) 447–466, https://doi.org/10.1006/jsvi.1993.1085.

[47] D.J. Thompson, N. Vincent, Track dynamic behaviour at high frequencies. Part 1: theoretical models and laboratory measurements, Vehicle System Dynamics 24 (sup1) (1995) 86–99, https://doi.org/10.1080/00423119508969617.